Spatial dynamic metabolomics identifies metabolic cell fate trajectories in human kidney differentiation

Wang, G.Q.; Heijs, B.; Kostidis, S.; Rietjens, R.G.J.; Koning, M.; Yuan, L.S.; ... ; Rabelink, T.J.

Cell Stem Cell

Resource

Spatial dynamic metabolomics identifies metabolic cell fate trajectories in human kidney differentiation

Graphical abstract

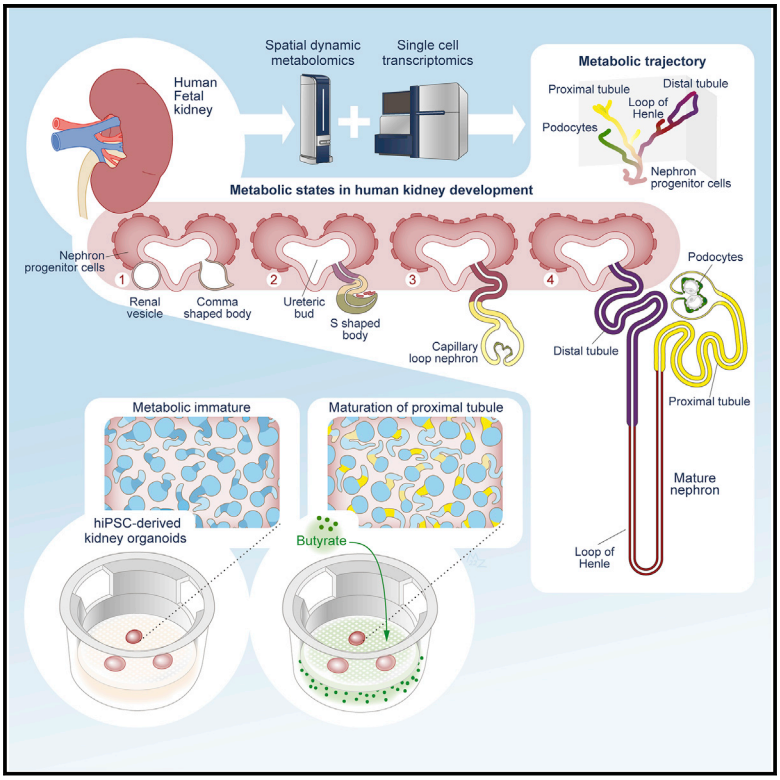

Highlights

- Kidney epithelium development follows metabolic trajectories
- Proximal tubular development shows a shift from glycolysis to fatty acid β-oxidation
- Kidney organoids show a metabolic immature phenotype in the absence of CPT1a expression
- Butyrate enhances proximal tubular maturation in kidney organoids

Authors

Gangqi Wang, Bram Heijs, Sarantos Kostidis, ..., Cathelijne W. van den Berg, Bernard M. van den Berg, Ton J. Rabelink

Correspondence

a.j.rabelink@lumc.nl

In brief

In this study, Wang et al. report metabolic trajectories during human kidney epithelium development using spatial dynamic metabolomics. This knowledge can be used to enhance proximal tubule differentiation and maturation in hiPSC-derived kidney organoids.

Wang et al., 2022, Cell Stem Cell *29*, 1580–1593
November 3, 2022
https://doi.org/10.1016/j.stem.2022.10.008

CellPress

CellPress
OPEN ACCESS

Cell Stem Cell

Resource

Spatial dynamic metabolomics identifies metabolic cell fate trajectories in human kidney differentiation

Gangqi Wang,[1,2] Bram Heijs,[2,3] Sarantos Kostidis,[3] Rosalie G.J. Rietjens,[1] Marije Koning,[1] Lushun Yuan,[1] Gesa L. Tiemeier,[1] Ahmed Mahfouz,[4,5] Sébastien J. Dumas,[1,2,6] Martin Giera,[2,3] Jesper Kers,[7] Susana M. Chuva de Sousa Lopes,[2,8] Cathelijne W. van den Berg,[1,2] Bernard M. van den Berg,[1] and Ton J. Rabelink[1,2,9,*]

[1]Department of Internal Medicine (Nephrology) & Einthoven Laboratory of Vascular and Regenerative Medicine, Leiden University Medical Center, Leiden, the Netherlands
[2]The Novo Nordisk Foundation Center for Stem Cell Medicine (reNEW), Leiden University Medical Center, the Netherlands
[3]Center of Proteomics and Metabolomics, Leiden University Medical Center, Leiden, the Netherlands
[4]Leiden Computational Biology Center, Leiden University Medical Center, Leiden, the Netherlands
[5]Delft Bioinformatics Lab, Delft University of Technology, Delft, the Netherlands
[6]Laboratory of Angiogenesis and Vascular Metabolism, Department of Oncology and Leuven Cancer Institute (LKI), KU Leuven, VIB Center for Cancer Biology, VIB, Leuven 3000, Belgium
[7]Department of Pathology, Leiden University Medical Center, Leiden, the Netherlands
[8]Department of Anatomy and Embryology, Leiden University Medical Center, Leiden, the Netherlands
[9]Lead contact
*Correspondence: a.j.rabelink@lumc.nl
https://doi.org/10.1016/j.stem.2022.10.008

SUMMARY

Accumulating evidence demonstrates important roles for metabolism in cell fate determination. However, it is a challenge to assess metabolism at a spatial resolution that acknowledges both heterogeneity and cellular dynamics in its tissue microenvironment. Using a multi-omics platform to study cell-type-specific dynamics in metabolism in complex tissues, we describe the metabolic trajectories during nephrogenesis in the developing human kidney. Exploiting *in situ* analysis of isotopic labeling, a shift from glycolysis toward fatty acid β-oxidation was observed during the differentiation from the renal vesicle toward the S-shaped body and the proximal tubules. In addition, we show that hiPSC-derived kidney organoids are characterized by a metabolic immature phenotype that fails to use mitochondrial long-chain fatty acids for energy metabolism. Furthermore, supplementation of butyrate enhances tubular epithelial differentiation and maturation in cultured kidney organoids. Our findings highlight the relevance of understanding metabolic trajectories to efficiently guide stem cell differentiation.

INTRODUCTION

With the advent of human induced pluripotent stem cells (hiPSCs) and differentiation protocols, the prospect of rebuilding human tissues for therapy has become apparent (Takasato et al., 2015). While the perspective to use such tissue for disease modeling and as therapeutic tissue product looks promising, substantial challenges remain. These include the generation of sufficient tissue, prevention and reduction of off-target differentiation, and enhanced on-target differentiation and maturation. Detailed knowledge of normal embryonic development is crucial to establish the framework within the organoid-based therapeutic strategies can be developed. This is especially true for organs as complex as the human kidney. Its functional unit, the nephron, is composed of over ten different types of epithelial cells with supporting vascular and stromal areas that are composed of an even larger array of different cell types (Humphreys, 2018). Comprehending this complex organ during development and in health and disease has proven to be intricate. Identification of therapeutic targets even more so (Humphreys, 2018).

Metabolism has been proposed as driver of cell differentiation during development, where intermediates of glycolysis, oxidative phosphorylation, and other biosynthetic pathways have been implicated in epigenetic control (Rabelink and Carmeliet, 2018). Metabolism acts as a fate determinant in asymmetric division of epithelial stem-like cells through selective inheritance of mitochondria (Dohla et al., 2022). In the healthy adult kidney, metabolic pathways vary widely from one cell type to another, with tubular epithelial cells depending on mitochondrial respiration and podocytes relying on glycolysis (Bhargava and Schnellmann, 2017; Brinkkoetter et al., 2019). In the fetal kidney, a delicate balance between self-renewal and differentiation of nephron progenitor cells (NPCs) is critical, where NPC self-renewal is supported by high glycolytic flux (Liu et al., 2017). In

CellPress
OPEN ACCESS

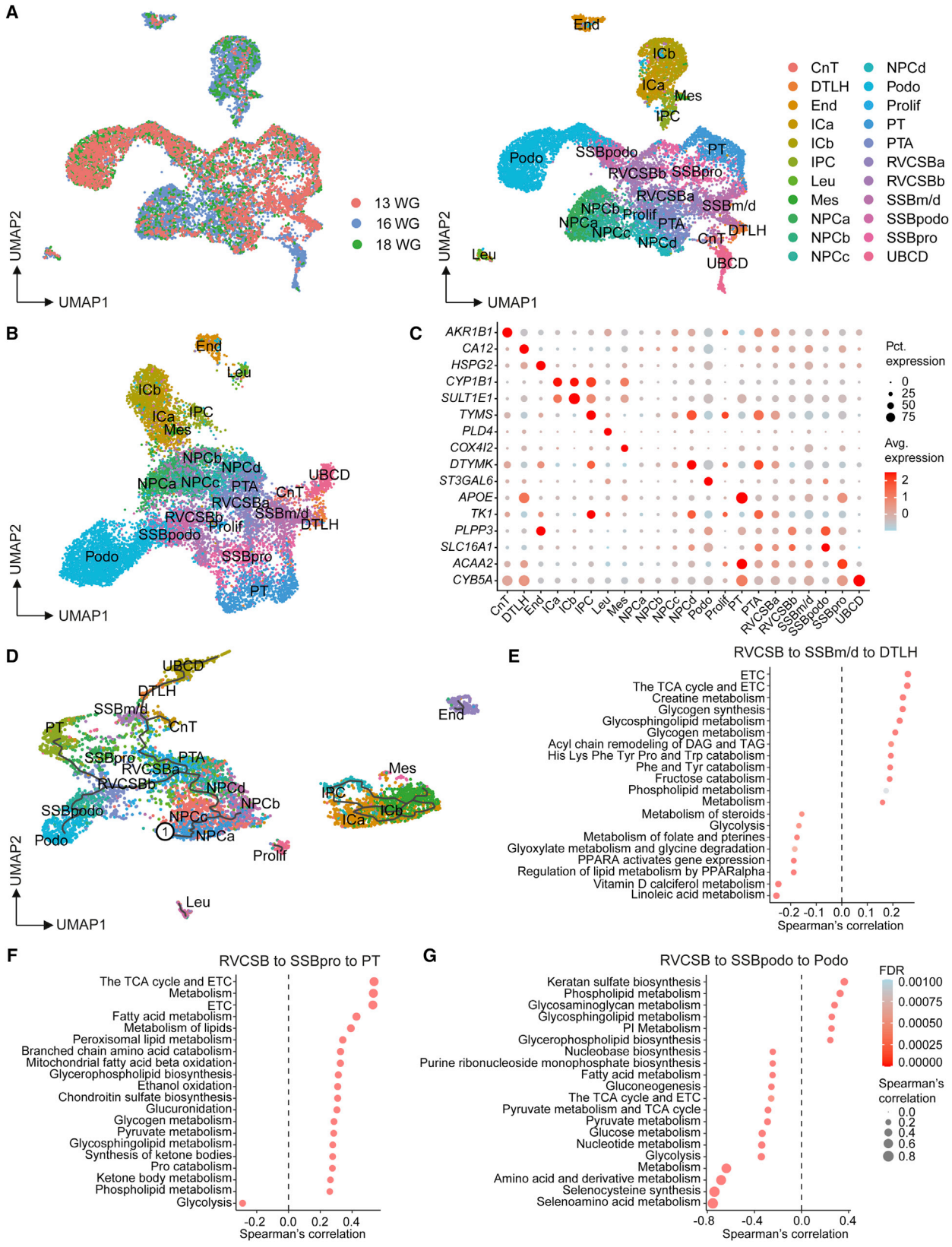

(legend on next page)

ischemic kidney injury, glycolysis is shown to be re-activated in the tubular epithelium (Lan et al., 2016), suggesting metabolic mimicry between embryonic NPC function and the repairing tubular epithelium. However, these results all either are obtained from mouse studies or focus on isolated cell types. An integrated understanding of the mechanisms underlying metabolic processes during human kidney development that acknowledges the heterogeneous cell complexity of the kidney will be crucial to identifying compounds and strategies that can improve endogenous or exogenous kidney regeneration.

Recently, we have descripted a cell-type-specific spatial dynamic metabolomics platform using high-spatial-resolution ($5 \times 5\ \mu m^2$ pixel size) matrix-assisted laser desorption/ionization mass spectrometry imaging (MALDI-MSI) combined with isotope tracing (Wang et al., 2022). This platform allows us to study dynamic changes in central carbon metabolism and nutrient partitioning in targeted cell types at subcellular resolution in the complex heterogeneous kidney tissue. Here, we further developed this platform into a multi-omics approach by combining the spatial dynamic metabolomics with single-cell RNA sequencing to characterize dynamic cellular metabolism in association with phenotypic and transcriptomic characteristics. We provide a metabolic atlas of the developing human kidney and explore its application to enhance kidney organoid differentiation from hiPSCs.

RESULTS

Metabolic heterogeneity and trajectory of renal cells in human fetal kidney

Cell metabolism is characteristically heterogeneous between different cell types and organs. To explore the metabolic heterogeneity of renal cells in the developing kidney, we first made a metabolic gene landscape of the developing kidney using our preprocessed single-cell transcriptomics data of human fetal kidneys from a previous report (Hochane et al., 2019). A total of 22 cell types were identified from three human fetal kidneys of different ages: 13 weeks, 16 weeks, and 18 weeks of gestation (WG), which cover all the developmental stages of nephrogenesis, such as NPCs, pre-tubular aggregate (PTA), renal vesicle (RV), comma-shaped body (CSB), S-shaped body (SSB), and mature glomerular and tubular epithelium (Figures 1A and S1A). Metabolic gene set enrichment based on Reactome pathway analysis was performed on the single-cell RNA-sequencing dataset and resulted in a dataset of 2,066 metabolic genes (Jassal et al., 2020). All the 22 different kidney cell types were characterized with unique metabolic gene patterns (Figure 1B). For example, *APOE* is highly expressed in proximal tubule (PT) and involved in lipid metabolism (Figure 1C). *SLC16A1* is highly expressed in podocytes of the S-shaped stage (SSBpodo), which encodes monocarboxylate transporter 1 and mediates the transmembrane transportation of monocarboxylates, such as lactate and short-chain fatty acids (SCFAs; Figure 1C). Pseudotime analysis of the metabolic gene dataset revealed that differentiation of NPCs toward each mature nephron component has a specific metabolic trajectory and can also identify the intermediate cell types in the differentiation process (Figure 1D). This developing trajectory on metabolic gene dataset is consistent with the previous report on the whole gene dataset (Hochane et al., 2019). It suggests that metabolic changes are indeed relevant to cell transition during kidney development. Furthermore, distal, proximal, and podocyte epithelium development were accompanied by distinct metabolic pathway changes, including central energy metabolism and lipid remodeling (Figures 1E–1G).

Spatial metabolomics revealing metabolic heterogeneity of renal cells in human fetal kidney

We then applied high-spatial-resolution MALDI-MSI to detect the spatial metabolome and lipidome directly on fresh frozen 16 WG human fetal kidney tissue at subcellular spatial resolution ($5 \times 5\ \mu m^2$ pixel size, with the average renal cell diameter of approximately 10 μm) (Figure S1B). The MALDI-MSI analyzed tissues were subsequently stained and imaged using multiplexed immunofluorescence microscopy. Microscopy images were co-registered to the MALDI-MSI data, which allowed for the molecular characterization of the different cell types present during kidney development. Multiplexed immunofluorescence staining was performed on human fetal kidney, which allowed for the identification of the different renal cell types based on both JAG1, WT1, and ECAD (encoded by gene *CDH1*) expression and morphology of the renal structures, as shown by single-cell transcriptomics data as well as previous reports (Lindstrom et al., 2018, 2021) (Figures 2A and S1C–S1H). Although distal tubule (DT), collecting duct (CD), and ureteric bud (UB) are all ECAD-positive epithelium, they were distinguished by their different positioning and structure, which, more importantly, was confirmed by distinct lipid signatures in the later analysis. Ultimately, a MALDI-MSI dataset containing approximately 544 tissue-specific *m/z* features representing the combined

Figure 1. Human renal cell metabolic heterogeneity characterized by single-cell transcriptomics

(A) Uniform manifold approximation and projection (UMAP) plot revealing 22 distinct renal cell types from three human fetal kidneys (13 WG, 16 WG, and 18 WG) detected by single-cell RNA sequencing. Colors represent kidney age (left) or cell type (right).

(B) UMAP plot visualizing different cell types from three human fetal kidneys based on metabolic gene expression only.

(C) Dot plot showing the main differentially expressed metabolic genes for each cell type.

(D) Embedding of 16 WG fetal kidney cells with trajectory analysis based on metabolic genes to show the developmental track based on their metabolism, colored by cell type. Starting point of the trajectory is labeled 1.

(E–G) Graphs showing top 20 metabolic pathways by Spearman's correlation between pseudotime score and pathway activity score during distal epithelium (E), proximal epithelium (F), and podocyte (G) development.

Abbreviations: NPC, nephron progenitor cell; IPC, interstitial progenitor cell; UB, ureteric bud; CD, collecting duct cell; CnT, connecting tubule; DTLH, distal tubule/loop of Henle; PT, proximal tubule; Podo, podocyte; PTA, pre-tubular aggregate cell; RVCSBa, renal vesicle/comma-shaped body cell a; RVCSBb, renal vesicle/comma-shaped body cell b; SSBm/d, S-shaped body cell medial/distal; SSBpro, S-shaped body cell proximal; SSBpodo, S-shaped body cell podocytes; IC, interstitial cell; End, endothelial cell; ICa, interstitial cell a; ICb, interstitial cell b; Leu, leukocyte; Mes, mesangial cell; Prolif, proliferating cell; TCA, the tricarboxylic acid cycle; ETC, respiratory electron transport chain.

CellPress
OPEN ACCESS

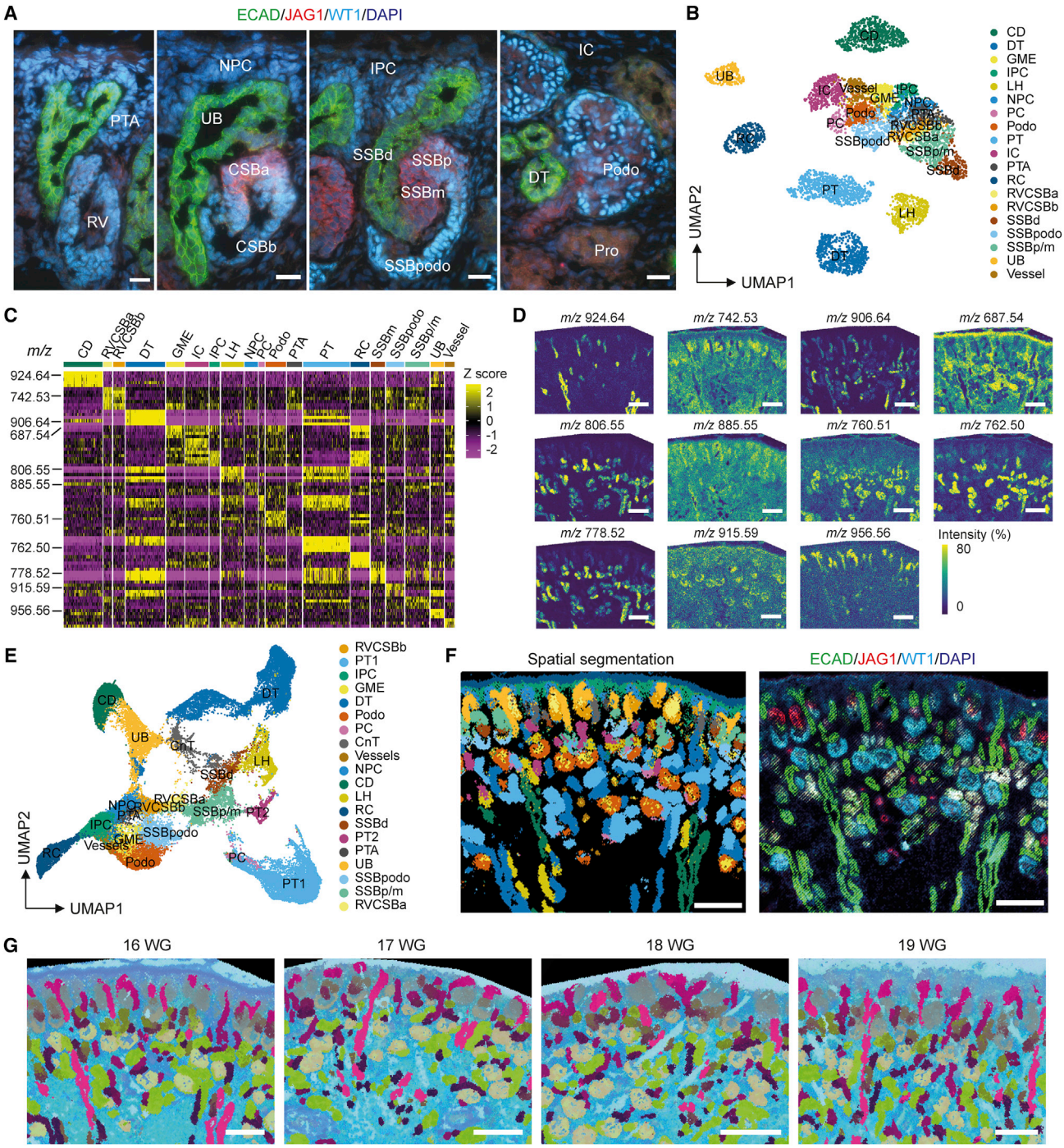

Figure 2. Human renal cell metabolic heterogeneity characterized by spatial metabolomics

(A) Immunofluorescence staining (ECAD [encoded by gene *CDH1*], JAG1, and WT1; scale bar, 20 μm) staining of 16 WG human fetal kidney tissue to identify cell types.

(B) UMAP map of 6,052 pixels extracted from 16 WG human fetal kidney MALDI-MSI data to visualize the metabolite and lipid heterogeneity within different renal cells. Pixels were selected and cell types identified after co-registration using the post-MALDI-MSI immunofluorescent staining.

(C) Heatmap of top 5 abundant signature metabolites and lipids abundance in different types of renal cells.

(D) Micrograph of cell-type-specific lipid species distribution as recorded by MALDI-MSI at 5 × 5 μm^2 pixel size in 16 WG human fetal kidney; *m/z* 924.64 (PE-NMe2(46:6) [M + Na-2H]$^-$), *m/z* 742.53 (PE-NMe2(34:2)/PE(36:2)/PC(33:2)/PE-NMe(35:2) [M−H]$^-$), *m/z* 906.64 (PS(40:0) [M + HAc-H]$^-$), *m/z* 687.54 (SM(d33:1) [M−H]$^-$), *m/z* 806.55 (Sulfatide(d36:1) [M−H]$^-$), *m/z* 885.55 (PI(38:4) [M−H]$^-$), *m/z* 760.51 (PS(34:1) [M−H]$^-$), *m/z* 762.50 (PE(38:6)/PE-NMe2(36:6)/PE-NMe(37:6) [M−H]$^-$), *m/z* 778.52 (Sulfatide(d34:1) [M−H]$^-$), *m/z* 915.59 (PI(40:4) [M−H]$^-$), *m/z* 956.56 (PG(LTE4/i-21:0)/PG(LTE4/a-21:0) [M-H2O-H]$^-$). Scale bar, 200 μm.

(legend continued on next page)

metabolome and lipidome and JAG1, WT1, and ECAD staining on the same tissue section were combined to establish a cell-type-specific *in situ* metabolomics dataset for the analysis of spatial metabolic heterogeneity in renal cell development.

In a semi-supervised approach, MALDI-MSI-derived metabolome and lipidome were exported for renal structures from 19 cell types after co-registration with immunofluorescence staining. Considering the accuracy of the image co-registration, we attempted to avoid the pixels from the border area of the renal structures. The combined spatial metabolome and lipidome appeared to be specific for the different developmental stages of the renal cells (Figure 2B), confirming the metabolic heterogeneity of renal cells in the developing kidney. Molecular features assigned to lipid species were shown to be most informative for cell type identification, as 68 of 81 signatures shown in Figure 2C are with $m/z > 500$ (Figures 2C and 2D). For example, m/z 762.50 (PE(38:6)/PE-NMe2(36:6)/PE-NMe(37:6) $[M-H]^-$) shows a specificity for PTs; m/z 915.59 (PI(40:4) $[M-H]^-$) is specific for podocytes; m/z 924.64 (PE-NMe2(46:6) $[M + Na\text{-}2H]^-$) is specific for CD; and m/z 956.56 (PG(LTE4/i-21:0)/PG(LTE4/a-21:0) $[M\text{-}H2O\text{-}H]^-$) is specific for UB (Figures 2C and 2D). In a non-supervised approach, the main kidney cell types in the 16 WG human fetal kidney could be accurately separated and retrospectively identified based on their spatial lipidome as confirmed by immunostaining-based cell-type identification (Figures 2E, 2F, and S1I). However, RVCSBa and RVCSBb were only partially separated in this approach because of their similarity in lipid profiles; therefore, we combined them as RVCSB in the following analysis. Unlike the single-cell transcriptomics dataset, which was not able to distinguish SSB distal and medial cells, spatial lipidome data were not able to separate SSB proximal and medial cells because of the limitation of immunostaining-based cell-type identification here. Nonetheless, both SSB proximal and medial cells will differentiate into proximal tubular cells (Lindstrom et al., 2021), which does not interfere with the following data analysis. Furthermore, the tested human fetal kidneys from different donors within a strict age range (16–19WG) showed similar lipid profiles (Figures 2G and S1J), which is consistent with the transcriptomics data as shown in Figure 1B (13–18WG), suggesting that the metabolic heterogeneity between renal cell types is relatively greater than possible differences in the measured age range. Therefore, we continued to study metabolic heterogeneity between renal cell types during nephrogenesis.

Lipid remodeling revealing human fetal kidney development trajectories *in situ*

Metabolic gene pathways involved in lipid remodeling were activated following development of PT, DT, and podocyte epithelium (Figures 1E–1G). In all three types of epithelial development, both phospholipid and glycosphingolipid metabolism pathways were increased, while the peroxisomal lipid metabolism pathway is mainly increased during PT development (Figures 1E–1G). To further explore lipid remodeling during kidney development, we applied pseudotime analysis on the spatial lipidome. The changes in spatial lipidome between different developmental phases from progenitor cells to the mature stages could be used to track the kidney development process (Figure 3A). The spatial trajectory map was also reflective of progressive epithelial development and maturation in different areas (Figures 3B–3D). For example, the pseudotime scores for the podocyte development branch were in line with the developmental stages from SSB, head-shaped body (HSB), and capillary loop stage (CLS) to mature podocytes (Figure 3E). In contrast, it was difficult to distinguish podocytes from HSB, CLS, and mature stage using transcriptomics data alone. From the early stages of differentiation to later stages (PTs, DTs, and podocytes), segment-specific cell-membrane-component (Eiersbrock et al., 2020) remodeling was displayed for each cell type, as revealed by lipid changes (Figures 3F–3H; Table S1).

To further highlight the capabilities of MALDI-MSI in identifying cell populations and assess their molecular maturation, we applied MALDI-MSI to a human nephroblastoma biopsy sample. Based on the MALDI-MSI-derived lipidome, the tumor biopsy displayed an immature fetal cell-like phenotype very similar to NPCs and cells in the RVCSB/SSB stages (Figures S2A and S2B). Moreover, trajectory analysis demonstrated a different spatial lipidome indicating potential off-target differentiation from the progenitor cell stage and without any further differentiation toward mature tubular structures (Figures S2C and S2D). This was consistent with histological examination (Figure S2E).

Metabolic switch during differentiation of proximal tubular epithelium

To study the dynamic metabolic changes and nutrient partitioning during fetal kidney development, we applied our recently described cell-type-specific spatial dynamic metabolomics platform on human fetal kidneys (Wang et al., 2022). In short, three fresh human fetal kidneys from different donors were sectioned into 350-μm-thick slices using a vibratome, followed by incubation with different ^{13}C-isotope-labeled nutrients for multiple durations up to 2 h, and the dynamic contribution of each ^{13}C-isotope labeled metabolite over time was measured in 10-μm-thick sections using MALDI-MSI at 5 × 5 μm^2 pixel-size resolution. Ultimately, a dynamic spatial metabolic dataset containing the complete ^{13}C-metabolite information from different time points and nutrients was established and projected on one tissue section through bioinformatic analysis (Figures S3A–S3D). This dataset was further combined with the single-cell transcriptomics dataset to achieve an improved multi-omics analysis.

(E) UMAP analysis on lipidomics data of 16 WG human fetal kidney samples. Pixels were selected in an unsupervised manner without co-registration to post-MALDI-MSI staining. Cell types were identified based on their molecular fingerprint as identified above and confirmed by immunofluorescent staining. Only the annotated renal cells are shown.

(F) Spatial segmentation (left) and post-MALDI-MSI staining (right) showing spatial lipid heterogeneity between different renal cells. Spatial segmentation colors match the color scheme of the UMAP in (E). Scale bar, 200 μm.

(G) Molecular histology of human fetal kidneys generated from integrated three-dimensional UMAP analysis of different datasets based on lipid profiles. Scale bar, 200 μm.

Abbreviations: SSBp/m, S-shaped body cell proximal/medial; PC, parietal epithelial cell; RC, renal capsule; GME, glomerular mesangial and endothelial cell.

CellPress
OPEN ACCESS

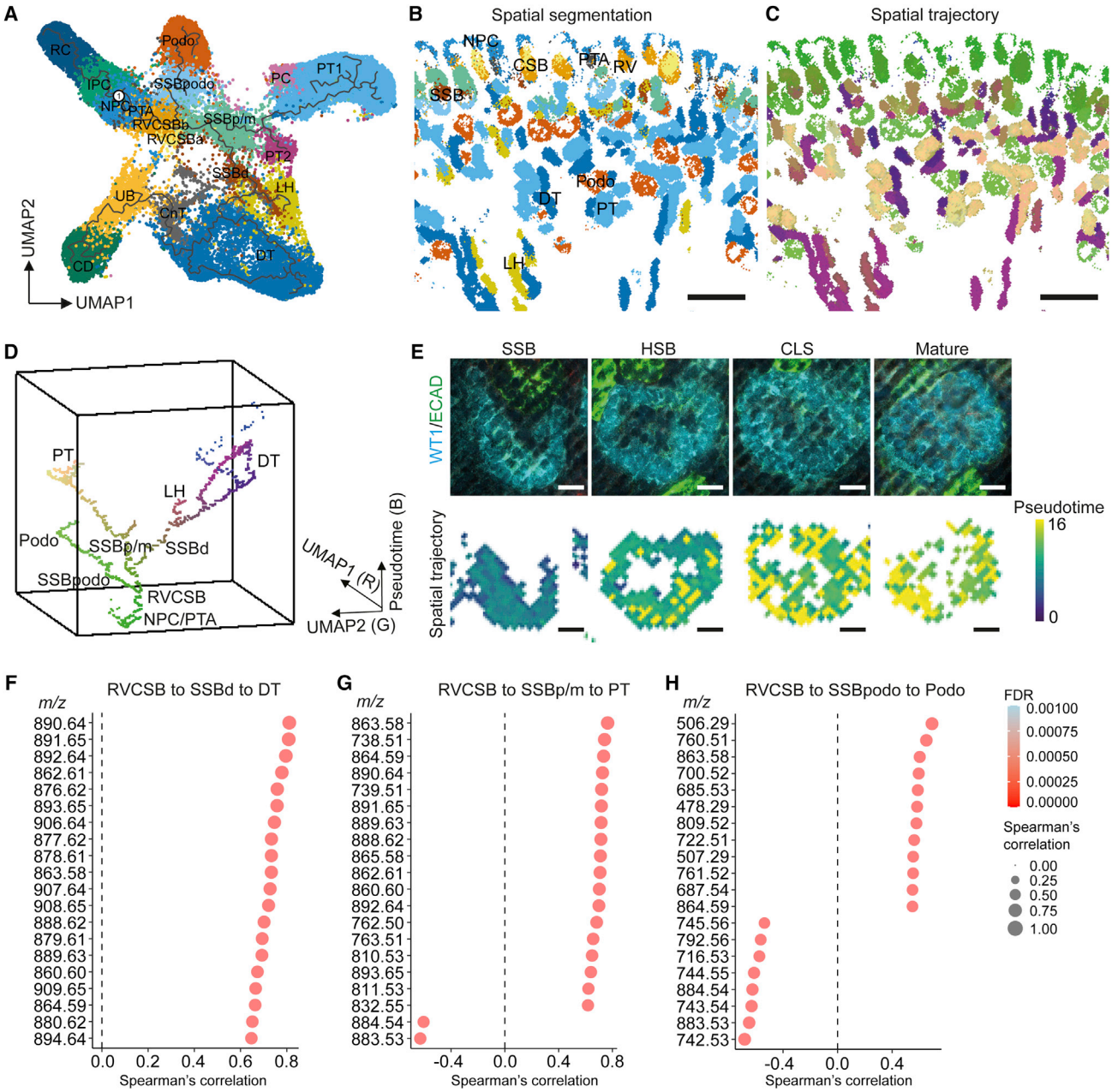

Figure 3. Pseudotime analysis clarifies developmental relationships between renal cell clusters

(A) Embedding of pixels from 16 WG human fetal kidney with trajectory analysis based on spatial lipidome to show the developmental track, colored by cell type. Starting point of the trajectory is labeled 1.

(B and C) Spatial segmentation (B) and spatial trajectory map (C) showing the pseudotime of fetal kidney development on tissue. Spatial segmentation colors match the color scheme in (A). Scale bar, 200 μm.

(D) 3D scatterplot showing the cell-type-specific trajectory generated from spatial trajectory map, with same color as the pixels shown in (C). Color scale represents pseudotime (blue), UMAP1 (red), and UMAP2 (green) generated from Monocle3.

(E) Detailed view of immunofluorescent staining and spatial trajectory showing maturation of podocytes from S-shaped body stage (SSB), head-shaped body stage (HSB), and capillary loop stage (CLS) to mature stage. Scale bar, 20 μm.

(F–H) Graphs showing top 20 *m/z* features by Spearman's correlation between pseudotime score and lipid abundance during distal epithelium (F), proximal epithelium (G), and podocyte (H) development.

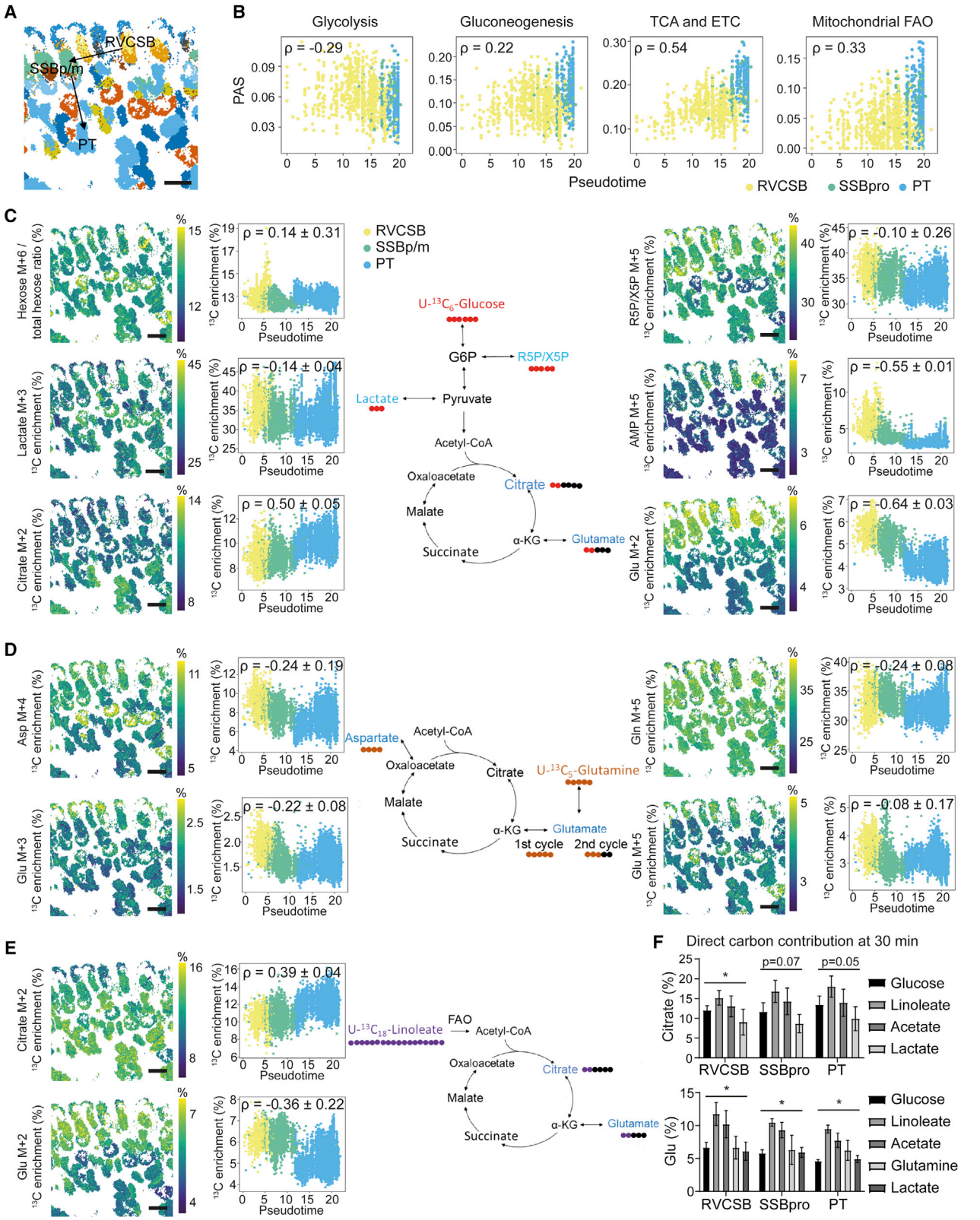

(legend on next page)

Differentiation of NPCs to PTA showed a gradual change of metabolic gene expression consistent with developmental progression (exemplified in Figure 1D). Based on the metabolic gene enrichment data, we observed that NPCs progressively change during differentiation with transcription of enzymes in both the TCA cycle and the respiratory electron transport chain (ETC) pathway being increasingly activated, resulting in a metabolic shift toward oxidative phosphorylation (Figures S4A and S4B). Transcription of essential enzymes in glucose, nucleotide, and amino acid metabolism pathways was activated during this metabolic shift (Figures S4A and S4B), providing the enzymes to produce both the energy and biomass precursors necessary for differentiation into proximal epithelium. Further differentiation from RVCSB and SSB to mature PT revealed a decreased expression of glycolysis pathway enzymes in combination with increased expression of enzymes of gluconeogenesis (Figures 4A and 4B). Pyruvate kinase (*PKM*), the rate-limiting glycolysis enzyme, decreased during this differentiation process (Figure S4C). Analyzing the spatial dynamic metabolomics data, mature PTs were shown to indeed have relatively lower $^{13}C_3$-lactate (lactate M+3) isotopologue enrichment without changing the total lactate level and higher $^{13}C_2$-citrate (citrate M+2) enrichment from glucose-derived carbons entering the TCA cycle compared to earlier developmental stages (Figures 4C,S3F, and S3G). The gene transcription for the oxidative phosphorylation pathways (TCA and ETC) were increasingly activated during proximal tubule development, accompanied by activation of the mitochondrial fatty acid β-oxidation (FAO) pathway (Figures 4A, 4B, and S4C). To establish whether the actual metabolism reflected the observed gene transcription patterns, we further evaluated the incorporation of ^{13}C from the labeled nutrients into TCA cycle intermediates. We observed the relative enrichment of U-$^{13}C_5$-glutamine-derived isotopologues, U-$^{13}C_5$-glutamate (Glu M+5), and $^{13}C_3$-glutamate (Glu M+3), which characterized one full cycle of the oxidative TCA cycle (Figure 4D). Activation of the oxidative TCA cycle in PT was indicated by the absence of $^{13}C_5$-citrate or $^{13}C_4$-glutamate at 1 h timescale, indicative of the reductive TCA cycle (Figures S3H and S3I). However, the U-$^{13}C_5$-glutamine and $^{13}C_3$-glutamate enrichment derived from U-$^{13}C_5$-glutamine supplementation were decreased in mature PT (Figure 4D). Furthermore, the contribution of U-$^{13}C_{18}$-linoleate to the enrichment of TCA cycle intermediate $^{13}C_2$-citrate through FAO was increased during proximal development (Figure 4E), which is in line with increased gene expression of *ACAA2*, catalyzing the last step of the mitochondrial FAO spiral (Figure S4C). Although we observed increased $^{13}C_2$-citrate enrichment from the contribution of both U-$^{13}C_6$-glucose and U-$^{13}C_{18}$-linoleate following the PT differentiation, its downstream $^{13}C_2$-glutamate enrichment was decreased, similar to what was observed from U-$^{13}C_5$-glutamine supplementation (Figures 4C–4E). Thus, we then looked into the gene expression data for whether citrate was being directed toward lipogenesis. The key enzyme genes (*ACLY* and *ACACA*) involved in *de novo* lipogenesis were decreased in mature PTs compared to SSB stage, which suggests lower use of excess citrate for lipogenesis in matured PTs (Figure S4D). Next, we examined whether the decrease of $^{13}C_2$-glutamate enrichment from U-$^{13}C_6$-glucose and U-$^{13}C_{18}$-linoleate is due to a higher influx of glutamate from other sources besides glutamine. One of such sources could be from the proline catabolism during PT development (Figure 1F). Indeed, we observed an increased expression in mature PTs for the key genes encoding the enzymes for the synthesis of glutamate from proline (Figure S4D), suggesting that this pathway could be more active in mature PTs. In that case, the influx of proline-derived glutamate could potentially explain the decrease of glutamate and glutamine ^{13}C enrichment. By combining all data, we found that the fatty acids U-$^{13}C_{18}$-linoleate and U-$^{13}C_2$-acetate are the main carbon source for the TCA cycle intermediates citrate and glutamate, rather than U-$^{13}C_6$-glucose, U-$^{13}C_5$-glutamine, and $^{13}C_3$-lactate, in all the PT developmental stages (Figure 4F). Compared to all the other renal cell types in human fetal kidney, PTs displayed higher FAO gene expression (*ACAA2* and *DBI*), linoleate abundance, and carbon contribution to citrate from linoleate (Figures S4E and S4F). Together, these data showed that a shift from glycolysis toward FAO is observed when following the differentiation from NPCs toward mature proximal epithelium.

Metabolic immaturity of hiPSC-derived kidney organoid proximal epithelium

We then sought to apply our insight in the metabolic trajectories analysis in the developing human kidney to examine proximal epithelium differentiation in hiPSC-derived kidney organoids. These tissues were generated using the protocol introduced by Takasato et al. (2015). The kidney organoids contain renal structures, such as glomeruli and proximal and distal tubular structures, as well as stromal cell populations and endothelial cells. First, we used our single-cell RNA-sequencing data on hiPSC-derived kidney organoids (Koning et al., 2022). A total of 23 cell types, including the main renal cell types PTs, DTs, and podocytes, were identified (Figure 5A). The annotated PT cell population expressed the well-known transcriptional factors *HNF4A*

Figure 4. Dynamic metabolic measurements on human fetal kidney proximal epithelial cells

(A) Spatial segmentation showing various renal cell types of human fetal kidney on tissue. Scale bar, 100 μm.

(B) Dot plots showing the pathway activity scores (PASs) for glycolysis, gluconeogenesis, TCA and ETC, and mitochondrial fatty acid oxidation (FAO) following trajectory of proximal epithelium development based on single-cell transcriptomics data.

(C) Images and dot plots showing the spatial dynamic metabolic measurements using U-$^{13}C_6$-glucose and their changes following trajectory of proximal epithelium development.

(D) Images and dot plots showing the dynamic metabolic measurements using U-$^{13}C_5$-glutamine and their changes following trajectory of proximal epithelium development.

(E) Images and dot plots showing the dynamic metabolic measurements using U-$^{13}C_{18}$-linoleate and their changes following trajectory of proximal epithelium development. Representative images and dot plots generated from 17 WG human fetal kidney are shown. Spearman correlation ρ is presented as mean ± SD calculated from 3 different human fetal kidneys (17 WG, 18 WG, and 19 WG). Scale bar, 100 μm. Color scale (%) represents the percentage of enrichment.

(F) Direct carbon contribution of different nutrients to citrate and glutamate at 30 min time point in proximal tubule cells as measured from the isotopologues citrate M+2, M+3, or glutamate M+2, M+3, and M+5. One-way ANOVA test, *$p < 0.05$.

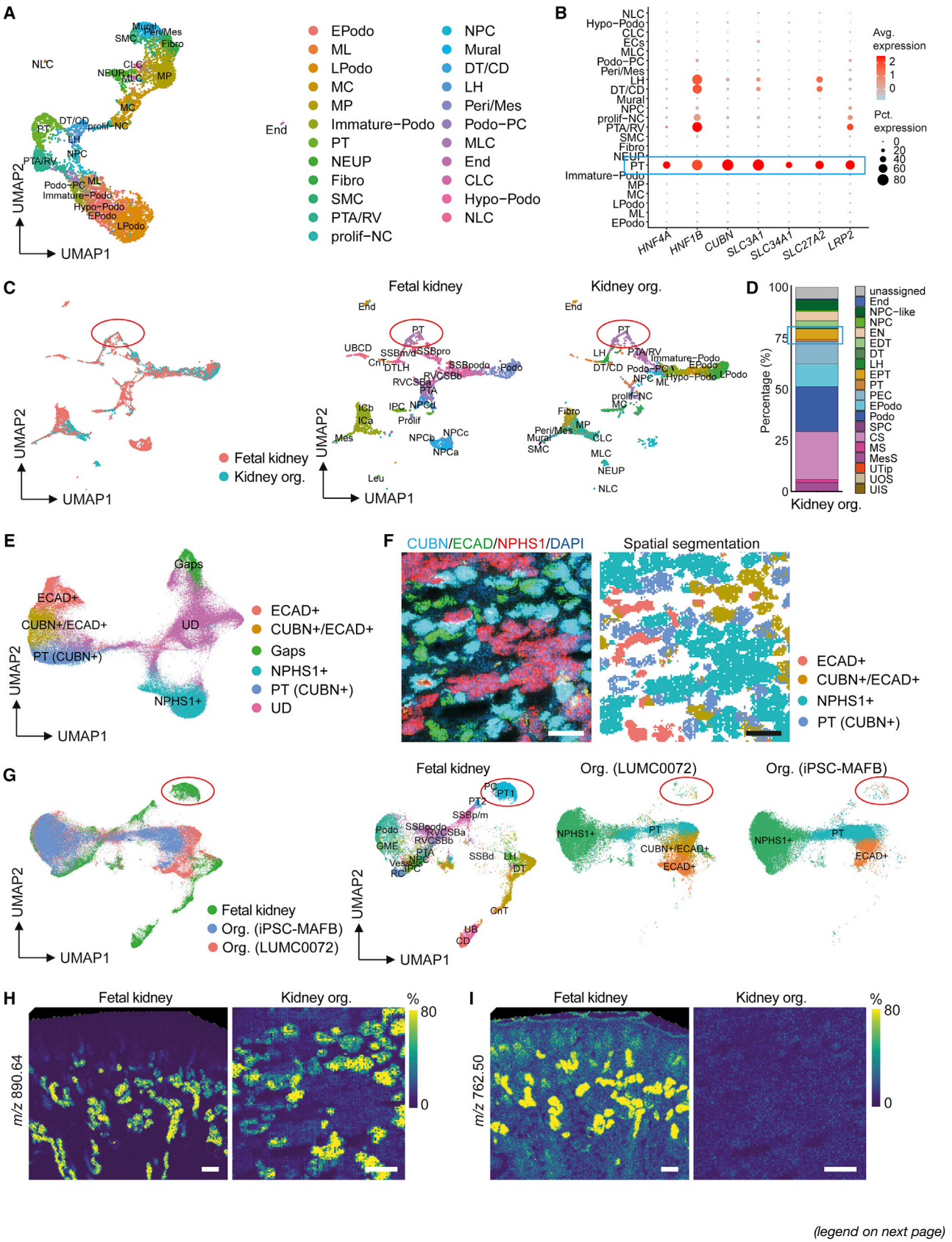

(legend on next page)

and *HNF1B* for kidney tubular development and the mature proximal epithelial markers *CUBN* and *SLC3A1* (Figure 5B). Kidney organoid PTs showed a similar gene transcription pattern as the human fetal kidney PTs (Figure 5C). Using the developing kidney cell classifier (DevKidCC) (Wilson et al., 2022), the existence of both early PT and mature PT cell populations were observed (Figure 5D). These data suggested that similar PT populations were observed in both hiPSC-derived kidney organoids and human fetal kidney.

We then applied MALDI-MSI measurements on hiPSC-derived kidney organoids differentiated from two hiPSC lines (LUMC0072 and iPSC-MAFB). The MALDI-MSI-derived spatial lipidome was able to identify the main renal structures in the kidney organoid including tubules and glomeruli (Figures 5E, 5F,S5A, and S5B). Kidney organoids from both cell lines had similar lipid patterns for the same cell types (Figures S5C and S5D). However, the overall lipidome fingerprint of the organoids, especially tubular structures, differed substantially from those obtained from human fetal kidney tissue (Figure 5G), most likely reflecting the immature state of kidney organoid tubular epithelium. In detail, although kidney organoids shared some signature lipid species for tubular structures with human fetal kidney, such as *m/z* 890.64 (3-*O*-Sulfogalactosylceramide (d42:1) $[M-H]^-$), they lacked the expression of other PT-specific lipid signatures highly abundant in the human fetal kidney, such as *m/z* 762.50 (PE(38:6)/PE-NMe2(36:6)/PE-NMe(37:6) $[M-H]^-$) (Figures 5H and 5I).

Butyrate selectively improves differentiation of proximal tubules in hiPSC-derived kidney organoids

During the development of PTs in the human fetal kidney, increased free fatty acid (FFA)-mediated mitochondrial oxidation was observed. Therefore, we explored the effect of FAO in hiPSC-derived kidney organoid on PT differentiation. Like human fetal kidney, both *ACAA2* and *DBI* genes were highly expressed in the PT of kidney organoids (Figure 6A). However, in contrast to PTs in human fetal and adult kidneys, the kidney organoid PTs lacked expression of CPT1, which is the rate-limiting transporter for long-chain fatty acid (LCFA) across the mitochondrial membrane to allow LCFA β-oxidation (Figures 6A, 6B, and S5E). Kidney organoid PTs do express MCT1, which is the transporter mediating SCFAs across the cell membrane (Figures 6B,S5F, and S5G). Unlike LCFAs, SCFAs can freely diffuse through the inner mitochondrial membrane and can thus be used for mitochondrial FAO without the need of active transport (Figure S5E). In line with the observed differential expression of CPT1 and MCT1, kidney organoids can use the SCFAs acetate and butyrate, but not linoleate, as a carbon source for the TCA cycle (Figures 6C and S5H). Butyrate, especially, could contribute very efficiently to this process when using the well-defined medium for isotope tracing as described in the STAR Methods section, while in the normal kidney organoid culture, medium 200 μM of acetate is already present without both LCFAs and butyrate (Table S2). To investigate whether *in vitro* differentiation can be enhanced through supplementation with SCFAs in the culture medium compared with the standard cultured kidney organoids without treatment, the addition of 500 μM butyrate to the regular culture medium selectively increased the percentage of fetal kidney-like proximal tubular epithelial cells over all tubular cells in the kidney organoids compared with control (Figures 6D and 6E). These epithelial cells were shown to colocalize with CUBN staining (Figure 6F), confirming their functional phenotype. Butyrate-treated kidney organoid PTs further showed a higher abundance of the PT signature lipid species *m/z* 740.52 (PE-NMe(35:3)/PE-NMe2(34:3)/PE(36:3)/PC(33:3) $[M-H]^-$) and lower abundance of the non-tubule structure signature lipid *m/z* 839.56 (PS(40:4) $[M-H]^-$) compared with control kidney organoid PTs (Figures 6G, 6H, and S5I). However, it should be noted that expression of certain PT signature lipid species, such as *m/z* 762.50 (PE(38:6)/PE-NMe2(36:6)/PE-NMe(37:6) $[M-H]^-$) as shown in Figure 5I, were still lacking after butyrate addition. To confirm the maturation of PTs after butyrate treatment, we further measured the gene expression of PT markers (Figure 5B) on fluorescence-activated cell sorted (FACS) LTL^+ proximal tubular cells (Figure S5J). Despite the observed variation in gene expression between different batches of kidney organoids as reported previously (Phipson et al., 2019), all the detected

Figure 5. Lipid heterogeneity and immaturity of hiPSC-derived kidney organoids proximal epithelial cells

(A) UMAP plot revealing 23 distinct cell types from hiPSC-derived kidney organoids (iPSC-MAFB) measured by single-cell RNA sequencing.

(B) Dot plots showing selected transcriptional factors (*HNF4A* and *HNF1B*) and maker genes (*CUBN*, *SLC3A1*, *SLC34A1*, *SLC27A2*, and *LRP2*) for proximal epithelium.

(C) UMAP analysis on integrated single-cell transcriptomics data of 16 WG human fetal kidney and kidney organoids (org.).

(D) ComponentPlot showing the classification of renal cells from kidney organoid single-cell transcriptomics data using developing kidney cell classifier (DevKidCC).

(E) UMAP analysis on lipidomics data of 6 different kidney organoids (LUMC0072) from 3 independent differentiations.

(F) Representative post-MALDI-MSI staining (left) and spatial segmentation (right) showing lipid heterogeneity between different renal cells in kidney organoid. Spatial segmentation colors are the same as the color scheme in (E). Scale bar, 100 μm.

(G) UMAP analysis on integrated lipidomics data of 16 WG human fetal kidney and 6 kidney organoids (3 LUMC0072 and 3 iPSC-MAFB) from 3 independent differentiations for each cell line showing lipid heterogeneity.

(H and I) Comparison of *m/z* 890.64 (3-*O*-Sulfogalactosylceramide (d42:1) $[M-H]^-$) (H) and *m/z* 762.50 (PE(38:6)/PE-NMe2(36:6)/PE-NMe(37:6) $[M-H]^-$) (I) distribution in human fetal kidney and kidney organoid. Scale bar, 100 μm. The color scale is based on the highest peak intensity within the two groups, which was set to 100%.

Abbreviations: EPodo, early podocyte; ML, mesenchymal-like cell; LPodo, late podocyte; MC, mesenchymal cell; MP, mesenchymal progenitor; Immature-Podo, immature podocyte; NEUP, neural progenitor; Fibro, fibroblast; SMC, smooth muscle cell; prolif-NC, proliferating nephron cell; Mural, unspecified mural cell; Peri/Mes, pericyte/mesangial cell; Podo-PC, podocyte-committed progenitor; MLC, melanocyte-like cell; CLC, chondrocyte-like cell; Hypo-Podo, hypoxic podocyte; NLC, neuron-like cell; UTip, ureteric tip; UOS, ureteric outer stalk; UIS, ureteric inner stalk; SPC, stromal progenitor cell; CS, cortical stroma; MS, medullary stroma; MesS, mesangial cell; EN, early nephron; EDT, early distal tubule; EPT, early proximal tubule; PEC, parietal epithelial cell; UrEp, ureteric epithelium; UD, undefined cells.

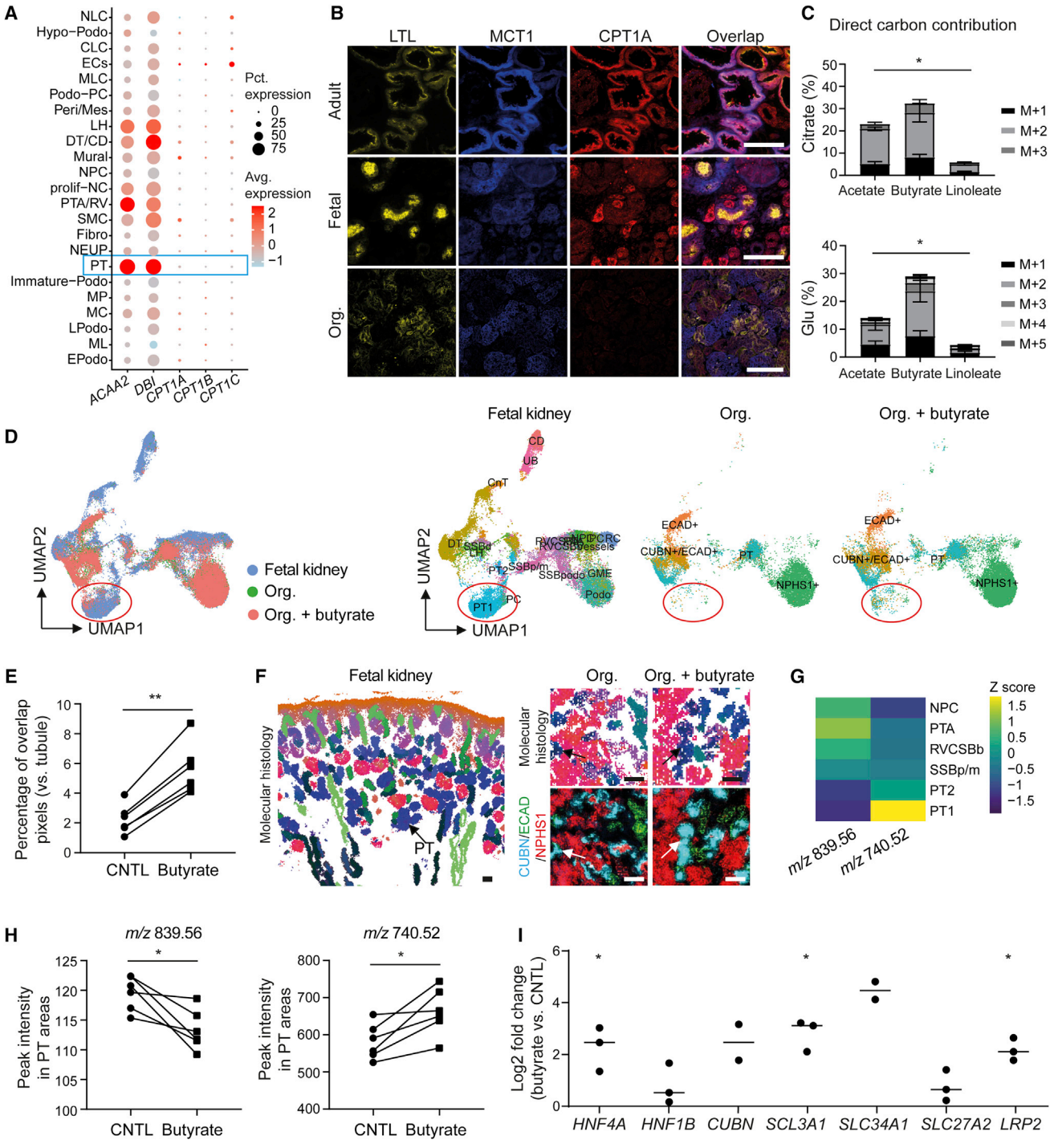

Figure 6. Butyrate improves proximal tubular cell differentiation in kidney organoids

(A) Dot plot showing gene expression of *ACAA2*, *DBI*, *CPT1A*, *CPT1B*, and *CPT1C* in different cell types of kidney organoid.

(B) Immunofluorescent (LTL, MCT1, and CPT1A) staining on human adult kidney, human fetal kidney, and hiPSC-derived kidney organoid. Scale bar, 100 μm.

(C) Direct carbon contribution of U-$^{13}C_2$-acetate, U-$^{13}C_4$-butyrate, or U-$^{13}C_{18}$-linoleate to citrate and glutamate at 4 h time point in kidney organoids (LUMC0072). 26 different organoids from 3 independent differentiations were measured. One-way ANOVA test, *$p < 0.05$.

(D) UMAP analysis on integrated lipidomics data of 16 WG human fetal kidney, kidney organoids, and kidney organoids treated with butyrate. The clusters of proximal tubular cells are labeled. 12 different organoids (LUMC0072, 6 per group) from 3 independent differentiations were analyzed. Only one representative kidney organoid per group was shown.

(E) The percentage of tubular cell pixels from kidney organoids overlapping with proximal tubular cells in human fetal kidney over total tubular cell pixels. Two-tailed paired t test, **$p < 0.01$.

(legend continued on next page)

genes were increased upon butyrate treatment (Figure 6I). Furthermore, the addition of 2 mM acetate to organoids increased the PT marker genes expression similarly to that observed after butyrate addition (Figure S5K). In summary, SCFAs can selectively improve differentiation of PTs in hiPSC-derived kidney organoids.

DISCUSSION

In this study, we describe a multi-omics analysis that allows for *in situ* cell-type-specific metabolomics in tissues. Combining dynamic spatial metabolomics with single-cell transcriptional analysis allows the comprehensive study of various metabolic pathways in complex tissues. We applied this platform to the developing human kidney and have created a high-resolution atlas that describes metabolic trajectories during human kidney development. Our comprehensive dataset shows nephron segment-specific changes in energy and lipid metabolism in the developing kidney, pointing toward the relevance for metabolism in cell fate transition during this complex developmental process. To this end, our multi-omics analysis gives in-depth insights into the spatial and temporal activity of metabolic programming during human nephrogenesis. In this study, we show that such insights can be applied to control and enhance differentiation of tissues derived from hiPSCs.

The use of hiPSC-derived kidney organoids to model kidney disease or to generate transplantable kidney tissue is currently hampered by lack of maturation as well as off-target stromal cell differentiation. We previously demonstrated that upon transplantation under the kidney capsule, such organoids could be advanced significantly in their maturation state upon vascularization (van den Berg et al., 2018, 2020). However, stromal populations in the kidney organoid that are still uncommitted to epithelial differentiation may differentiate along other stromal lineages (Wu and Humphreys, 2020) upon prolonged culture or during the hypoxic interval toward vascularization when transplanted. We hypothesized that based on our identified metabolic trajectories in human kidney development, the culture environment could be adapted to support selective differentiation of nephron segments. To this end, we increased SCFA availability during kidney organoid differentiation, which, based on our multi-omics analysis, appear as key nutrients during the maturation of PTs. In support of this hypothesis, we have demonstrated increased PT differentiation after medium supplementation with acetate and butyrate.

This dataset also provides an unprecedented single-cell-resolution identification of the different cell types in complex tissues based on its spatial lipidome. This is exemplified by the nephroblastoma tissue where the spatial lipidome of the tumor tissue clustered together with a specific developmental stage of nephrogenesis. This highlights that this approach may be of wider relevance to the field of tumor biology to identify the ontogeny of its cellular components (Abdelmoula et al., 2016; Balluff et al., 2015). Because of the limitation of the lipid identification approach used in this study, we only reported the lipid class with the total carbon content and fatty-acid saturation for all the possible lipids corresponding to the detected *m/z* ratio. For further confirmation of lipid identification, tandem MS approach or validation with reference standards need to be performed. As the molecular histology shows the information of hundreds of lipids within one figure, it is a promising tool to add functional information to classical histology. To this end, we introduced the combination of such analysis with immunofluorescent (IF) staining (Goossens et al., 2022).

The development of single-cell approaches to uncover the transcriptome of kidney cells, one cell at a time, has opened opportunities to uncover cellular heterogeneity in health and in disease and to spotlight their specialization associated with the multiple roles they have in the human kidney (Clark et al., 2019; Hochane et al., 2019; Liao et al., 2020; Young et al., 2018). Integration of metabolomics data will be another important steppingstone to refine insight in cellular heterogeneity. Here, we proposed a multi-omics approach by combining cell-type-specific spatial dynamic metabolomics with single-cell transcriptomics data, which allows us to study the metabolic cellular heterogeneity in depth. The here-created multi-omics metabolic atlas of human fetal kidney may serve as a basis to design interventions that can promote renal repair and regeneration.

Limitation of this study

While we postulated that butyrate bypasses the absence of CPT1a in the mitochondria to drive the TCA cycle and hence differentiation in kidney organoids, we cannot infer the final mechanism of action from our data. Interestingly, coupling of fatty-acid-driven oxidative phosphorylation in renal epithelium to nuclear receptor (estrogen-related receptor alpha and peroxisomal proliferation-activated receptor alpha) activation has been reported (Dhillon et al., 2021). However, we cannot exclude alternative mechanism of action for butyrate and acetate, like histone modification during kidney organoids differentiation (Soliman and Rosenberger, 2011; Ware et al., 2009). Finally, while our method combines high-resolution spatial metabolic information with dynamic isotope tracing during kidney development, the labeling studies were limited to 2 h, which currently precludes a full downstream labeling of all metabolic intermediates and hence a full understanding of the interplay of glycolysis and TCA cycle with other cellular metabolic pathways. In addition, other isotope tracers are needed to detail specific pathways

(F) Molecular histology generated from 3D UMAP analysis on integrated lipidomics data of 16 WG human fetal kidney (left) and kidney organoids (right). Pixels with similar lipid profile from different samples are showing similar color. Immunofluorescent staining on post-MALDI-MSI kidney organoids is shown on the lower panel. Scale bar, 50 μm.

(G) Heatmap showing the abundance of *m/z* 839.56 (PS(40:4) $[M-H]^-$) and *m/z* 740.52 (PE-NMe(35:3)/PE-NMe2(34:3)/PE(36:3)/PC(33:3) $[M-H]^-$) in different cell types following the development of proximal epithelium.

(H) Graphs showing the changes of *m/z* 839.6 and *m/z* 740.6 abundance in proximal epithelium after treatment with butyrate. Two-tailed paired t test, $^*p < 0.05$.

(I) Graph showing the changes of proximal tubular cell marker gene expression of fluorescence-activated cell sorted (FACS) LTL + proximal epithelial cells after treatment with butyrate. One-sample t test, $^*p < 0.05$.

such as glutamate metabolism derived from other sources, like. for example, from proline catabolism.

STAR★METHODS

Detailed methods are provided in the online version of this paper and include the following:

- KEY RESOURCES TABLE
- RESOURCE AVAILABILITY
  - Lead contact
  - Materials availability
  - Data and code availability
- EXPERIMENTAL MODEL AND SUBJECT DETAILS
  - Human samples
  - Cell lines
- METHOD DETAILS
  - Maintenance and differentiation of hiPSCs
  - Kidney organoid dissociation and flow cytometry sorting
  - RNA isolation and RT-PCR
  - Vibratome sectioning and tissue slice incubation
  - Tissue preparation and matrix deposition
  - MALDI-MSI measurement
  - Immunofluorescence staining
  - MSI data processing and analysis
  - Single cell RNA-seq analysis
  - Nuclear magnetic resonance (NMR) metabolomics
- QUANTIFICATION AND STATISTICAL ANALYSIS

SUPPLEMENTAL INFORMATION

Supplemental information can be found online at https://doi.org/10.1016/j.stem.2022.10.008.

ACKNOWLEDGMENTS

The Novo Nordisk Foundation Center for Stem Cell Medicine (reNEW) is supported by Novo Nordisk Foundation grants (NNF21CC0073729). G.W. was financially supported by Prof. Jaap de Graeff-Lingling Wiyadharma subsidy of the Leiden University Fund (LUF) and the China Scholarship Council grant. Financial support by Marie Skłodowska-Curie Individual Fellowship to Sebastien J. Dumas is gratefully acknowledged. Financial support by the China Scholarship Council grant to Lushun Yuan is gratefully acknowledged. We thank Ellen Lievers (LUMC, Leiden, the Netherlands) for technical assistance. We thank Christian Freund (hiPSC core facility, LUMC, Leiden, the Netherlands) for providing cell line LUMC0072iCTRL01 and Melissa Little (Murdoch Children's Research Institute, Melbourne, Australia) for iPSC-MAFB. We are grateful to the staff of the Vrelinghuis, Utrecht, for their efforts in obtaining the human fetal material as well as the donors that have consented for the use of the material. We thank Manon Zuurmond (LUMC, Leiden, the Netherlands) for illustration of graphical abstract.

AUTHOR CONTRIBUTIONS

G.W. designed research study, conducted experiments, acquired data, and wrote the manuscript. B.H. provided the technical guidance of MALDI-MSI experiments and data processing and wrote the manuscript. S.M.C.d.S.L. provided human fetal kidney tissues and single-cell RNA-sequencing data, read the manuscript, and provided helpful comments. L.Y. helped with the data analysis, read the manuscript, and provided helpful comments. S.K. conducted NMR experiments and analysis, read the manuscript, and provided expert knowledge on isotope-tracing analysis. R.G.J.R. and G.L.T. read the manuscript and provided helpful comments. A.M. provided professional instruction of single-cell data analysis, read the manuscript, and provided helpful comments. M.K. and S.J.D. provided the single-cell RNA-sequencing data of kidney organoids, read the manuscript, and provided helpful comments. M.G. provided expert knowledge on cell metabolism, read the manuscript, and provided helpful comments. J.K. provided the nephroblastoma tissue, read the manuscript, and provided helpful comments. C.W.v.d.B. provided hiPSC-derived kidney organoids, conducted experiments, acquired data, read the manuscript, and provided helpful comments. B.M.v.d.B. and T.J.R. designed the research study, interpreted the data, and wrote the manuscript.

DECLARATION OF INTERESTS

The authors declare no competing interests.

Received: August 18, 2022
Revised: October 7, 2022
Accepted: October 17, 2022
Published: November 3, 2022

REFERENCES

Abdelmoula, W.M., Balluff, B., Englert, S., Dijkstra, J., Reinders, M.J.T., Walch, A., McDonnell, L.A., and Lelieveldt, B.P.F. (2016). Data-driven identification of prognostic tumor subpopulations using spatially mapped t-SNE of mass spectrometry imaging data. Proc. Natl. Acad. Sci. USA *113*, 12244–12249. https://doi.org/10.1073/pnas.1510227113.

Balluff, B., Frese, C.K., Maier, S.K., Schone, C., Kuster, B., Schmitt, M., Aubele, M., Hofler, H., Deelder, A.M., Heck, A.J., et al. (2015). De novo discovery of phenotypic intratumour heterogeneity using imaging mass spectrometry. J. Pathol. *235*, 3–13. https://doi.org/10.1002/path.4436.

Bhargava, P., and Schnellmann, R.G. (2017). Mitochondrial energetics in the kidney. Nat. Rev. Nephrol. *13*, 629–646. https://doi.org/10.1038/nrneph.2017.107.

Brinkkoetter, P.T., Bork, T., Salou, S., Liang, W., Mizi, A., Ozel, C., Koehler, S., Hagmann, H.H., Ising, C., Kuczkowski, A., et al. (2019). Anaerobic Glycolysis Maintains the Glomerular Filtration Barrier Independent of Mitochondrial Metabolism and Dynamics. Cell Rep. *27*, 1551–1566.e5. https://doi.org/10.1016/j.celrep.2019.04.012.

Clark, J.Z., Chen, L., Chou, C.L., Jung, H.J., Lee, J.W., and Knepper, M.A. (2019). Representation and relative abundance of cell-type selective markers in whole-kidney RNA-Seq data. Kidney Int. *95*, 787–796. https://doi.org/10.1016/j.kint.2018.11.028.

Dhillon, P., Park, J., Hurtado Del Pozo, C., Li, L., Doke, T., Huang, S., Zhao, J., Kang, H.M., Shrestra, R., Balzer, M.S., et al. (2021). The Nuclear Receptor ESRRA Protects from Kidney Disease by Coupling Metabolism and Differentiation. Cell Metab. *33*, 379–394.e8. https://doi.org/10.1016/j.cmet.2020.11.011.

Dohla, J., Kuuluvainen, E., Gebert, N., Amaral, A., Englund, J.I., Gopalakrishnan, S., Konovalova, S., Nieminen, A.I., Salminen, E.S., Torregrosa Muñumer, R., et al. (2022). Metabolic determination of cell fate through selective inheritance of mitochondria. Nat. Cell Biol. *24*, 148–154. https://doi.org/10.1038/s41556-021-00837-0.

Eiersbrock, F.B., Orthen, J.M., and Soltwisch, J. (2020). Validation of MALDI-MS imaging data of selected membrane lipids in murine brain with and without laser postionization by quantitative nano-HPLC-MS using laser microdissection. Anal. Bioanal. Chem. *412*, 6875–6886. https://doi.org/10.1007/s00216-020-02818-y.

Goossens, P., Lu, C., Cao, J., Gijbels, M.J., Karel, J.M., Wijnands, E., Claes, B.S., Fazzi, G.E., Hendriks, T.F., Wouters, K., et al. (2022). Integrating multiplex immunofluorescent and mass spectrometry imaging to map myeloid heterogeneity in its metabolic and cellular context. Cell Metab. *34*, 1214–1225.e6. https://doi.org/10.1016/j.cmet.2022.06.012.

Heinrich, P., Kohler, C., Ellmann, L., Kuerner, P., Spang, R., Oefner, P.J., and Dettmer, K. (2018). Correcting for natural isotope abundance and tracer impurity in MS-MS/MS- and high-resolution-multiple-tracer-data from stable

isotope labeling experiments with IsoCorrectoR. Sci. Rep. *8*, 17910. https://doi.org/10.1038/s41598-018-36293-4.

Hochane, M., van den Berg, P.R., Fan, X., Bérenger-Currias, N., Adegeest, E., Bialecka, M., Nieveen, M., Menschaart, M., Chuva de Sousa Lopes, S.M., and Semrau, S. (2019). Single-cell transcriptomics reveals gene expression dynamics of human fetal kidney development. PLoS Biol. *17*, e3000152. https://doi.org/10.1371/journal.pbio.3000152.

Huang, J., Liang, X., Xuan, Y., Geng, C., Li, Y., Lu, H., Qu, S., Mei, X., Chen, H., Yu, T., et al. (2017). A reference human genome dataset of the BGISEQ-500 sequencer. GigaScience *6*, 1–9. https://doi.org/10.1093/gigascience/gix024.

Humphreys, B.D. (2018). Mapping kidney cellular complexity. Science *360*, 709–710. https://doi.org/10.1126/science.aat7271.

Jassal, B., Matthews, L., Viteri, G., Gong, C., Lorente, P., Fabregat, A., Sidiropoulos, K., Cook, J., Gillespie, M., Haw, R., et al. (2020). The reactome pathway knowledgebase. Nucleic Acids Res. *48*, D498–D503. https://doi.org/10.1093/nar/gkz1031.

Koning, M., Dumas, S.J., Avramut, M.C., Koning, R.I., Meta, E., Lievers, E., Wiersma, L.E., Borri, M., Liang, X., Xie, L., et al. (2022). Vasculogenesis in kidney organoids upon transplantation. Npj Regen. Med. *7*, 40. https://doi.org/10.1038/s41536-022-00237-4.

Korostin, D., Kulemin, N., Naumov, V., Belova, V., Kwon, D., and Gorbachev, A. (2020). Comparative analysis of novel MGISEQ-2000 sequencing platform vs Illumina HiSeq 2500 for whole-genome sequencing. PLoS One *15*, e0230301. https://doi.org/10.1371/journal.pone.0230301.

Lan, R., Geng, H., Singha, P.K., Saikumar, P., Bottinger, E.P., Weinberg, J.M., and Venkatachalam, M.A. (2016). Mitochondrial Pathology and Glycolytic Shift during Proximal Tubule Atrophy after Ischemic AKI. J. Am. Soc. Nephrol. *27*, 3356–3367. https://doi.org/10.1681/asn.2015020177.

Liao, J., Yu, Z., Chen, Y., Bao, M., Zou, C., Zhang, H., Liu, D., Li, T., Zhang, Q., Li, J., et al. (2020). Single-cell RNA sequencing of human kidney. Sci. Data *7*, 4. https://doi.org/10.1038/s41597-019-0351-8.

Lindstrom, N.O., Sealfon, R., Chen, X., Parvez, R.K., Ransick, A., De Sena Brandine, G., Guo, J., Hill, B., Tran, T., Kim, A.D., et al. (2021). Spatial transcriptional mapping of the human nephrogenic program. Dev. Cell *56*, 2381–2398.e6. https://doi.org/10.1016/j.devcel.2021.07.017.

Lindstrom, N.O., Tran, T., Guo, J., Rutledge, E., Parvez, R.K., Thornton, M.E., Grubbs, B., McMahon, J.A., and McMahon, A.P. (2018). Conserved and Divergent Molecular and Anatomic Features of Human and Mouse Nephron Patterning. J. Am. Soc. Nephrol. *29*, 825–840. https://doi.org/10.1681/asn.2017091036.

Liu, J., Edgington-Giordano, F., Dugas, C., Abrams, A., Katakam, P., Satou, R., and Saifudeen, Z. (2017). Regulation of Nephron Progenitor Cell Self-Renewal by Intermediary Metabolism. J. Am. Soc. Nephrol. *28*, 3323–3335. https://doi.org/10.1681/asn.2016111246.

Phipson, B., Er, P.X., Combes, A.N., Forbes, T.A., Howden, S.E., Zappia, L., Yen, H.J., Lawlor, K.T., Hale, L.J., Sun, J., et al. (2019). Evaluation of variability in human kidney organoids. Nat. Methods *16*, 79–87. https://doi.org/10.1038/s41592-018-0253-2.

Qiu, X., Mao, Q., Tang, Y., Wang, L., Chawla, R., Pliner, H.A., and Trapnell, C. (2017). Reversed graph embedding resolves complex single-cell trajectories. Nat. Methods *14*, 979–982. https://doi.org/10.1038/nmeth.4402.

Rabelink, T.J., and Carmeliet, P. (2018). Renal metabolism in 2017: Glycolytic adaptation and progression of kidney disease. Nat. Rev. Nephrol. *14*, 75–76. https://doi.org/10.1038/nrneph.2017.173.

Soliman, M.L., and Rosenberger, T.A. (2011). Acetate supplementation increases brain histone acetylation and inhibits histone deacetylase activity and expression. Mol. Cell. Biochem. *352*, 173–180. https://doi.org/10.1007/s11010-011-0751-3.

Stuart, T., Butler, A., Hoffman, P., Hafemeister, C., Papalexi, E., Mauck, W.M., Hao, Y., Stoeckius, M., Smibert, P., and Satija, R. (2019). Comprehensive Integration of Single-Cell Data. Cell *177*, 1888–1902.e21. https://doi.org/10.1016/j.cell.2019.05.031.

Takasato, M., Er, P.X., Chiu, H.S., Maier, B., Baillie, G.J., Ferguson, C., Parton, R.G., Wolvetang, E.J., Roost, M.S., Chuva de Sousa Lopes, S.M., and Little, M.H. (2015). Kidney organoids from human iPS cells contain multiple lineages and model human nephrogenesis. Nature *526*, 564–568. https://doi.org/10.1038/nature15695.

van den Berg, C.W., Koudijs, A., Ritsma, L., and Rabelink, T.J. (2020). In Vivo Assessment of Size-Selective Glomerular Sieving in Transplanted Human Induced Pluripotent Stem Cell-Derived Kidney Organoids. J. Am. Soc. Nephrol. *31*, 921–929. https://doi.org/10.1681/asn.2019060573.

van den Berg, C.W., Ritsma, L., Avramut, M.C., Wiersma, L.E., van den Berg, B.M., Leuning, D.G., Lievers, E., Koning, M., Vanslambrouck, J.M., Koster, A.J., et al. (2018). Renal Subcapsular Transplantation of PSC-Derived Kidney Organoids Induces Neo-vasculogenesis and Significant Glomerular and Tubular Maturation In Vivo. Stem Cell Rep. *10*, 751–765. https://doi.org/10.1016/j.stemcr.2018.01.041.

Vanslambrouck, J.M., Wilson, S.B., Tan, K.S., Soo, J.Y.C., Scurr, M., Spijker, H.S., Starks, L.T., Neilson, A., Cui, X., Jain, S., et al. (2019). A Toolbox to Characterize Human Induced Pluripotent Stem Cell-Derived Kidney Cell Types and Organoids. J. Am. Soc. Nephrol. *30*, 1811–1823. https://doi.org/10.1681/asn.2019030303.

Wang, G., Heijs, B., Kostidis, S., Mahfouz, A., Rietjens, R.G.J., Bijkerk, R., Koudijs, A., van der Pluijm, L.A.K., van den Berg, C.W., Dumas, S.J., et al. (2022). Analyzing cell-type-specific dynamics of metabolism in kidney repair. Nat. Metab. *4*, 1109–1118. https://doi.org/10.1038/s42255-022-00615-8.

Ware, C.B., Wang, L., Mecham, B.H., Shen, L., Nelson, A.M., Bar, M., Lamba, D.A., Dauphin, D.S., Buckingham, B., Askari, B., et al. (2009). Histone deacetylase inhibition elicits an evolutionarily conserved self-renewal program in embryonic stem cells. Cell Stem Cell *4*, 359–369. https://doi.org/10.1016/j.stem.2009.03.001.

Wilson, S.B., Howden, S.E., Vanslambrouck, J.M., Dorison, A., Alquicira-Hernandez, J., Powell, J.E., and Little, M.H. (2022). DevKidCC allows for robust classification and direct comparisons of kidney organoid datasets. Genome Med. *14*, 19. https://doi.org/10.1186/s13073-022-01023-z.

Wishart, D.S., Feunang, Y.D., Marcu, A., Guo, A.C., Liang, K., Vazquez-Fresno, R., Sajed, T., Johnson, D., Li, C., Karu, N., et al. (2018). HMDB 4.0: the human metabolome database for 2018. Nucleic Acids Res. *46*, D608–D617. https://doi.org/10.1093/nar/gkx1089.

Wu, H., and Humphreys, B.D. (2020). Single Cell Sequencing and Kidney Organoids Generated from Pluripotent Stem Cells. Clin. J. Am. Soc. Nephro. *15*, 550–556. https://doi.org/10.2215/cjn.07470619.

Young, M.D., Mitchell, T.J., Vieira Braga, F.A., Tran, M.G.B., Stewart, B.J., Ferdinand, J.R., Collord, G., Botting, R.A., Popescu, D.M., Loudon, K.W., et al. (2018). Single-cell transcriptomes from human kidneys reveal the cellular identity of renal tumors. Science *361*, 594–599. https://doi.org/10.1126/science.aat1699.

STAR★METHODS

KEY RESOURCES TABLE

REAGENT or RESOURCE	SOURCE	IDENTIFIER
Antibodies		
Mouse monoclonal anti-ECAD	BD Biosciences	Cat # 610181; RRID:AB_397580
Goat polyclonal anti-JAG1	R&D Systems	Cat # AF1277; RRID:AB_354713
Rabbit polyclonal anti-WT-1	Santa Cruz	Cat # sc-192; RRID:AB_632611
Rabbit polyclonal anti-CUBN	Invitrogen, Thermo-Fisher	Cat # PA5-83684; RRID:AB_2790837
Rabbit polyclonal anti-SLC3A1	Proteintech	Cat # 16343-1-AP; RRID:AB_2239419
Rabbit polyclonal anti-MCT1	Proteintech	Cat # 20139-1-AP; RRID:AB_2878645
Mouse monoclonal anti-CPT1A	Abcam	Cat # ab128568; RRID:AB_11141632
Sheep polyclonal anti-NPHS1	R&D Systems	Cat # AF4269; RRID:AB_2154851
Biological samples		
Human fetal kidney tissue from elective abortion	Acquired from Human Anatomy, Leiden University Medical Center, Leiden, The Netherlands (approved by the Medical Ethics Committee of the LUMC, P08.087)	N/A
Fresh-frozen human nephroblastoma sample (Wilms tumor)	Acquired from the pathology archives of the Amsterdam University Medical Center, location AMC (Amsterdam UMC) according to the Code of Conduct for responsible use (2011) by the Federation for Dutch Medical Scientific Societies (FEDERA)	N/A
hiPSC LUMC0072	https://hpscreg.eu	N/A
iPSC-MAFB	https://doi.org/10.1038/nprot.2018.007	N/A
Chemicals, peptides, and recombinant proteins		
Lotus Tetragonolobus Lectin (LTL)	Vector Laboratories	Cat # FL-1321-2
Vitronectin	Thermo Fisher Scientific	Cat # A14700
Essential 8 medium	Thermo Fisher Scientific	Cat # A1517001
Ultra-Pure 0.5M EDTA	Thermo Fisher Scientific	Cat # 15575020
TrypLE Select	Thermo Fisher Scientific	Cat # 12563011
RevitaCell	Thermo Fisher Scientific	Cat # A26445-01
CHIR99021	Tocris	Cat # 4423/10
STEMdiff APEL-2 medium	Stem Cell Technologies	Cat # 05275
PFHMII	Thermo Fisher Scientific	Cat # 12040-077
Antibiotic-antimycotic	Thermo Fisher Scientific	Cat # 15240062
rhFGF9	R&D Systems	Cat # 273-F9-025
Heparin	Sigma Aldrich	Cat #H3149-10KU
Sodium acetate	Sigma	Cat #S5636
Sodium butyrate	Sigma	Cat #B5887
Glucose/glutamine free DMEM medium	Gibco	Cat # A1443001
Fetal Bovine Serum	Gibco	Cat # 10270-106
Linoleic acid	Sigma Aldrich	Cat #L1376
BSA	Sigma Aldrich	Cat # A7030
Glucose	Gibco	Cat # 15023-21
Glutamine	Sigma Aldrich	Cat #G8540
Penicillin/streptomycin	Gibco	Cat # 15070-063
U-$^{13}C_{18}$- linoleic acid (98%)	Cambridge Isotope Laboratories, Inc.	Cat # CLM-6855-0
U-$^{13}C_2$-acetate (99%)	Cambridge Isotope Laboratories, Inc.	Cat # CLM-440-1

(*Continued on next page*)

Continued

REAGENT or RESOURCE	SOURCE	IDENTIFIER
U-$^{13}C_4$-butyrate (99%)	Cambridge Isotope Laboratories, Inc.	Cat # CLM-10426-0.1
U-$^{13}C_6$-glucose (99%)	Sigma	Cat # 389374
U-$^{13}C_2$-lactate (99%)	Cambridge Isotope Laboratories, Inc.	Cat # CLM-1579-0.1
U-$^{13}C_6$-glutamine (99%)	Cambridge Isotope Laboratories, Inc.	Cat # CLM-1822-H
Collagenase I	Worthington	Cat # LS004196
DNAse I	Sigma Aldrich	Cat #D4527
Dulbecco's PBS (DPBS)	Thermo Fisher Scientific	Cat # 14190094
Trizol reagent	Life Technologies	Cat # 15596018
Oligo (dT) and dNTP	Promega	Cat #C110A
Hanks' Balanced Salt Solution (HBSS)	Gibco	Cat # 2458830
Agarose	Roche	Cat # 11388991001
N-(1-naphthyl) ethylenediamine dihydrochloride (NEDC)	Sigma Aldrich	Cat #N9125
Prolong™ gold antifade mountant with DAPI	ThermoFisher	Cat #P36931
100% LC-grade methanol	ACTU-All chemicals	Cat # UN1230
Critical commercial assays		
RNeasy mini kit	Qiagen	Cat # 74106
Rec. RNasin RNase inhibitor	Promega	Cat #N251B
SYBR select master mix	Applied Biosystems™	Cat # 4472897
Deposited data		
Raw MALDI-MSI data	This paper	Upon request
All the exported and processed MSI data together with data information in Figshare	This paper	Figshare Data: https://doi.org/10.6084/m9.figshare.20477256.v1
Code for analyzing MALDI-MSI data	This paper	Zenodo Data: https://doi.org/10.5281/zenodo.7191331
Human fetal kidney single cell RNA sequencing data	Hochane et al. (2019)	GEO: GSE114530
Kidney organoids single cell RNA sequencing data	Koning et al. (2022)	ArrayExpress database: E-MTAB-11429
Experimental models: Cell lines		
hiPSC LUMC0072	This paper	N/A
iPSC-MAFB	This paper	N/A
Experimental models: Organisms/strains		
Human fetal kidney tissue	This paper	N/A
Human nephroblastoma sample	This paper	N/A
Oligonucleotides		
Primers for RT-PCR, See Table S3.	This paper	N/A
Software and algorithms		
ftmsControl, version 2.1.0	Bruker Daltonics GmbH	N/A
flexImaging 5.0	Bruker Daltonics GmbH	N/A
SCiLS Lab 2016b	Bruker Daltonics GmbH	N/A
Human Metabolome Database	Wishart et al. (2018)	Human Metabolome Database: https://hmdb.ca/
MATLAB R2019a	MathWorks	N/A
Seurat	Stuart et al. (2019)	https://satijalab.org/seurat/
IsoCorrectoR	Heinrich et al. (2018)	https://bioconductor.org/packages/release/bioc/html/IsoCorrectoR.html

(*Continued on next page*)

Continued

REAGENT or RESOURCE	SOURCE	IDENTIFIER
Monocle3	Qiu et al. (2017)	https://cole-trapnell-lab.github.io/monocle3/
developing kidney cell classifier (DevKidCC)	Wilson et al. (2022)	https://kidneyregeneration.github.io/DevKidCC/index.html
Chenomx NMR suite 8.4	Chenomix NMR suite	N/A
Other		
FACSCanto II	BD Biosciences	N/A
Vibratome sectioning (Vibratome VT1200)	Leica Microsystems	VT1200
Cryosectioning (Cryostar NX70 cryostat)	Thermo Fisher	NX70
Indium-tin-oxide (ITO)-coated glass slides	VisionTek Systems Ltd.	N/A
SunCollect sprayer	SunChrom GmbH	N/A
RapifleX MALDI-TOF/TOF	Bruker Daltonics GmbH	N/A
12T SolariX FTICR mass spectrometer	Bruker Daltonics GmbH	N/A
3D Histech Pannoramic MIDI Scanner	Sysmex	N/A
Leica White Light Laser Confocal Microscope TCS SP8 using LAS-X Image software with 3D module	Leica	N/A
14.1 T (600 MHz for ^{1}H) Bruker Avance II NMR	Bruker Daltonics GmbH	N/A

RESOURCE AVAILABILITY

Lead contact

Further information and requests for resources and reagents should be directed to and will be fulfilled by the lead contact, Ton J. Rabelink (a.j.rabelink@lumc.nl).

Materials availability

This study did not generate new unique reagents.

Data and code availability

- This paper analyzes existing, publicly available single cell RNAseq datasets. These accession numbers for the datasets are listed in the key resources table. The raw MALDI-MSI data reported in this study cannot be deposited in a public repository because of the large data size. To request access, contact Gangqi Wang (g.wang@lumc.nl) or Bram Heijs (b.p.a.m.heijs@lumc.nl). All the exported and processed MALDI-MSI data together with data information have been deposited at Figshare. DOI is listed in the key resources table.
- Code used in the study has been deposited at Zenodo and is publicly available as of the date of publication. DOI is listed in the key resources table.
- Any additional information required to reanalyze the data reported in this paper is available from the lead contact upon request.

EXPERIMENTAL MODEL AND SUBJECT DETAILS

Human samples

The collection and use of human material in this study was approved by the Medical Ethics Committee of the Leiden University Medical Center (P08.087). The gestational age was determined by ultrasonography from women undergoing elective abortion. The material from four embryos (16-week, 17-week, 18-week and 19-week of gestation) was donated with written informed consent. In addition, an anonymized fresh-frozen nephroblastoma sample (Wilms tumor) was acquired from the pathology archives of the Amsterdam University Medical Center, location AMC (Amsterdam UMC) according to the Code of Conduct for responsible use (2011) by the Federation for Dutch Medical Scientific Societies (FEDERA).

Cell lines

hiPSCs (LUMC0072iCTRL01(LUMC0072, details at https://hpscreg.eu) and iPSC-MAFB (Vanslambrouck et al., 2019)) were maintained on vitronectin in Essential 8 medium (Thermo Fisher Scientific) using 0.5 mM Ultra-Pure EDTA (Thermo Fisher Scientific) at 37°C and 5% CO_2.

METHOD DETAILS

Maintenance and differentiation of hiPSCs

hiPSCs (LUMC0072iCTRL01(LUMC0072, details at https://hpscreg.eu) and iPSC-MAFB (Vanslambrouck et al., 2019)) were maintained on vitronectin in Essential 8 medium (Thermo Fisher Scientific) using 0.5 mM Ultra-Pure EDTA (Thermo Fisher Scientific) at 37°C and 5% CO_2. The day before differentiation was initiated, cells were split with TrypLE Select (Thermo Fisher Scientific) and plated in E8 supplemented with RevitaCell (Thermo Fisher Scientific). Differentiation was performed as described previously (Takasato et al., 2015; van den Berg et al., 2018). Briefly, cells were cultured for 4 days in 8 μM CHIR99021 (Tocris) in STEMdiff APEL-2 medium supplemented with 1% PFHMII (Life Technologies) and 1% Antibiotic-Antimycotic (Life Technologies) at 37°C and 5% CO_2. On day 4, medium was changed to APEL-2 containing 200 ng mL^{-1} rhFGF9 (R&D Systems) and 1 μg mL^{-1} heparin (Sigma-Aldrich). On day 7, cells were pulsed with 5 μM CHIR99021 for 1 h, dissociated and transferred to 3D organoid culture 0.4 μM transwell pore polyester membranes. Five days later, growth factors were removed and medium was changed every 2 days. Organoids were maintained on the transwell membranes for another two weeks from day 7 + 5 to 7 + 18 with treatment of 2 mM sodium acetate (S5636, Sigma) or 500 μM sodium butyrate (B5887, Sigma) in APEL-2 medium at 37°C and 5% CO_2. Three independent kidney organoid batches were collected for data acquisition.

For the isotope tracing experiments, kidney organoids at day 7 + 18 were incubated in a well-defined medium (Glucose free and glutamine free DMEM medium (Gibco, A1443001), supplemented with 2% FCS, 0.5 mM linoleic acid (dissolved with addition of 1% BSA), 5 mM glucose, 500 μM glutamine, 2 mM sodium acetate, 500 μM sodium butyrate and penicillin/streptomycin (pH adjusted to 7.4) for up to 4 h at 37°C and 5% CO_2. For the ^{13}C-labeling incubation, same amounts of either U-$^{13}C_{18}$- linoleic acid (98%, Cambridge Isotope Laboratories, Inc. CLM-6855-0), U-$^{13}C_2$-acetate (99%, Cambridge Isotope Laboratories, Inc. CLM-440-1) or U-$^{13}C_4$-butyrate (99%, Cambridge Isotope Laboratories, CLM-10426-0.1) were used to replace similar un-labeled nutrients in each medium. In the end, kidney organoids were quenched with liquid N2 and stored at −80°C.

Kidney organoid dissociation and flow cytometry sorting

Kidney organoids from LUMC0072 and hiPSC-MAFB were dissociated at day 7 + 17. Tissues were incubated at 37°C for 40 min in collagenase I buffer (600U mL^{-1} collagenase Type I (Worthington) and 0.75 U mL^{-1} DNAse (Sigma Aldrich) in HBSS with calcium and magnesium ($HBSS^{+/+}$, Thermo Fisher Scientific)). After centrifugation, the cell suspension was further dissociated to single cells at 37°C for 5 min in TrypLE buffer (5U mL^{-1} DNAse I and 4 μg mL^{-1} heparin (Sigma Aldrich) in 80% TrypLE select 10x (Thermo Fisher Scientific) in DPBS (Thermo Fisher Scientific)). The dissociation was ended by resuspension in in $HBSS^{+/+}$ with FCS. The cell pellet was resuspended in FACS buffer (0.1% BSA in PBS).

For flow cytometry analysis, dissociated cells were incubated with Lotus Tetragonolobus Lectin (LTL), Fluorescein (1:300, Vector Laboratories, FL-1321-2) and anti-MCT1 (1:50, Proteintech, 20139-1-AP) in FACS buffer for 30 min on ice. MCT1 was stained for 30 min at 4°C with anti-rabbit APC (1:500, Invitrogen, A21244). FACS analysis was performed using a FACSCanto II, FACSDiva Software and FlowJo (all BD Biosciences).

For flow cytometry sorting, dissociated cells were incubated with LTL FITC (1:300, Vector Laboratories, FL-1321-2) in FACS buffer for 30 min on ice and washed. Cells were sorted using a FACS Aria II 3L with FACSDiva Software (both BD Biosciences) and collected in FACS buffer. Dataplots were generated in FlowJo (BD Biosciences).

RNA isolation and RT-PCR

LTL positive cells after FACS sorting were harvested in Trizol reagent (Life Technologies, 15,596,018). Total RNA was isolated using RNeasy mini kit (Qiagen, 74,106) according to its protocol. cDNA was synthesized by mixing 1 mg total RNA, Oligo (dT) (Promega, C110A) and dNTP (Promega, C110A) and incubate at 65°C for 5 min firstly. Then M-MLV reverse transcriptase (Promega, M170B), recombinant RNasin RNase inhibitor (Promega, N251B) and DTT were added into the mixture and incubate at 37°C for 50 min. Terminate the reaction by incubating at 70°C for 15 min. SYBR select master mix (Applied BiosystemsTM, 4,472,897) and specific primers (Table S3) were used for real-time PCR. The expression of genes were determined by normalized to either *GAPDH* or *ARP* levels. Both normalization showed similar results. The values normalized to *ARP* level were shown in the figures.

Vibratome sectioning and tissue slice incubation

Human fetal kidneys were collected and kept in ice-cold sterile Hanks' Balanced Salt Solution (HBSS) with 5 mM glucose and penicillin/streptomycin before vibratome sectioning. Each kidney was embedded in 4% low temperature-melting agarose gel and 350 μm thick tissue slices were obtained from fresh tissue under ice-cold HBSS with 5mM glucose and penicillin/streptomycin using a Vibratome VT1200 (Leica Microsystems, Germany). Slicing speed was 0.1 mm/s, and vibration amplitude was 2 mm.

Tissue slices were placed into culture plates and incubated in a well-defined medium (Glucose free and glutamine free DMEM medium (Gibco, A1443001), supplemented with 2% FCS, 0.5 mM linoleic acid (dissolved with addition of 1% BSA), 5 mM glucose, 500 μM glutamine, 100 μM sodium acetate, 500 μM sodium lactate and penicillin/streptomycin (pH adjusted to 7.4) for up to 2 h at 37°C and 5% CO_2. During incubation, medium was changed to media containing various ^{13}C-labeled nutrients at different time points. For the ^{13}C-labeling incubation, same amounts of either U-$^{13}C_6$-glucose (99%, Sigma, 389,374), U-$^{13}C_6$-glutamine (99%, Cambridge Isotope Laboratories, Inc. CLM-1822-H), U-$^{13}C_{18}$- linoleic acid (98%, Cambridge Isotope Laboratories, Inc. CLM-6855-0), U-$^{13}C_2$-acetate (99%, Cambridge Isotope Laboratories, Inc. CLM-440-1) or U-$^{13}C_2$-lactate (98%, Cambridge Isotope

Laboratories, CLM-1579-0.1) were used to replace similar un-labeled nutrients in each medium. In the end, tissue slices were quenched with liquid N2 and stored at −80°C.

Tissue preparation and matrix deposition

Human fetal kidneys, nephroblastoma biopsy and kidney organoids were directly frozen using liquid nitrogen after being obtained, and stored at −80°C. Tissue was embedded in 10% gelatin and sections of 10 μm thickness were cryosectioned using a Cryostar NX70 cryostat (Thermo Fisher Scientific, MA, USA) at −20°C. The sections were thaw-mounted onto indium-tin-oxide (ITO)-coated glass slides (VisionTek Systems Ltd., Chester, UK). Mounted sections were placed in a vacuum freeze-dryer for 15 min prior to matrix application. After drying, *N*-(1-naphthyl) ethylenediamine dihydrochloride (NEDC) (Sigma-Aldrich, UK) MALDI-matrix solution of 7 mg/mL in methanol/acetonitrile/deionized water (70, 25, 5 %v/v/v) was applied using a SunCollect sprayer (SunChrom GmbH, Friedrichsdorf, Germany). A total of 21 matrix layers were applied with the following flowrates: layer 1-3 at 5 μL/min, layer 4-6 at 10 μL/min, layer 7-9 at 15 μL/min and 10-21 at 20 μL/min (speed *x*, medium 1; speed *y*, medium 1; *z* position, 35).

MALDI-MSI measurement

MALDI-TOF/TOF-MSI was performed using a RapifleX MALDI-TOF/TOF system (Bruker Daltonics GmbH, Bremen, Germany). Negative ion-mode mass spectra were acquired at a pixel size of 5 × 5 μm^2 in a mass range from *m/z* 80-1000 in reflection mode. Prior to analysis the instrument was calibrated using red phosphorus. Spectra were acquired with 15 laser shots per pixel at a laser repetition rate of 10 kHz. Data acquisition was performed using flexControl (Version 4.0, Bruker Daltonics, Germany) and visualizations were obtained from flexImaging 5.0 (Bruker Daltonics). All the samples from same slides were measured randomly. MALDI-FTICR-MSI was performed on a 12T solariX FTICR mass spectrometer (Bruker Daltonics GmbH, Bremen, Germany) in negative-ion mode, using 30 laser shots and 50 μm pixel size. Prior to analysis the instrument was calibrated using red phosphorus. The spectra were recorded in an *m/z* range of 100-1000 with a 2M data point transient and transient length of 0.5592 s. Data acquisition was performed using ftmsControl (Version 2.1.0, Bruker Daltonics), and visualizations were obtained from flexImaging 5.0 (Bruker Daltonics). Following the MALDI-MSI data acquisition, excess matrix was removed by washing in 100% ethanol (2 × 5 min), 75% ethanol (1 × 5 min) and 50% ethanol (1 × 5 min), after which this MSI-analyzed-tissue-section was used for immunofluorescence staining as described below.

Immunofluorescence staining

Tissues on the slide were fixed using 4% paraformaldehyde for 10 min, then blocked with 3% normal goat serum, 2% BSA and 0.01% Triton X-100 in PBS for 1 h at room temperature. Primary anti-ECAD antibody (1:300, BD Biosciences, 610,181), anti-JAG1 (10 μg/mL, R&D, AF1277), anti-WT1 (1:300, Santa Cruz, sc-192), anti-CUBN (1:300, Invitrogen, PA5-83684), anti-SLC3A1 (1:50, Proteintech, 16343-1-AP), anti-MCT1 (1:100, proteintech, 20139-1-AP), anti-CPT1A (5 μg/mL, abcam, ab128568) anti-NPHS1 (2 μg/mL, R&D, AF4269) or Lotus Tetragonolobus Lectin (LTL, 1:300, Vector Laboratories, Brunschwig Chemie, Amsterdam, The Netherlands, B-1325) were incubated overnight at 4°C, followed by corresponding fluorescent-labelled secondary antibodies (Invitrogen) for 1 h at 4°C. Slides were embedded in ProlongTM gold antifade mountant with DAPI (ThermoFisher, P36931). Fluorescent images of the slides were recorded using a 3D Histech Pannoramic MIDI Scanner (Sysmex, Etten-Leur, the Netherlands).

Whole 3-dimensional organoids were fixed using 2% paraformaldehyde for 20 min and blocked and permeabilized with 10% donkey serum in 0.3% Triton in PBS. Tissues were stained overnight at 4°C with antibodies: anti-Lotus Tetragonolobus Lectin (LTL, 1:300, Vector Laboratories, B-1325), anti-CUBN (1:300, Thermo Fisher Scientific, PA5-83684), anti-SLC3A1 (1:50, Proteintech, 16343-1-AP) or anti-MCT1 (1:100, Proteintech, 20139-1-AP) followed by secondary antibodies (Invitrogen) for 2 h at room temperature. Tissues were counterstained with Hoechst 33,342 (Thermo Fisher Scientific), embedded in Pro-Long Gold Antifade Mountant in 35 mm glass bottom dishes (MatTek corporation) and imaged using Leica White Light Laser Confocal Microscope TCS SP8 using LAS-X Image software with 3D module (Leica).

MSI data processing and analysis

MSI data were exported and processed in SCiLS Lab 2016b (SCiLS, Bruker Daltonics) with baseline correction using convolution algorithm. All MALDI-TOF-MSI data were normalized to the total ion count (TIC). Peak picking was performed (signal-to-noise-ratio > 3) on the average spectrum, and matrix peaks were excluded from the *m/z* feature list. The *m/z* features present in both MALDI-FTICR-MSI and MALDI-TOF-MSI datasets, and which had similar tissue distributions were further used for identity assignment of lipid species. The *m/z* values from MALDI-FTICR-MSI were imported into the Human Metabolome Database(Wishart et al., 2018) (https://hmdb.ca/) after re-calibration in mMass and annotated for lipids species with an error < ±5 ppm. For the small molecules detected only in MALDI-TOF, the *m/z* values from MALDI-TOF were imported into the Human Metabolome Database after re-calibration in mMass and annotated for metabolites with an error < ±20 ppm. The ^{13}C-labeled peaks were selected by comparing the spectrum of control and ^{13}C-labeling experiments, and annotated based on the presence of un-labeled metabolites and their theoretical *m/z* values. Peak intensities of the selected features were exported for all the measured pixels from SCiLS Lab 2016b, which were used for the following analysis.

For the semi-supervised approach data analysis on 16 WG fetal kidney, the MALDI-MSI-based distribution of *m/z* 888.6, which shows specific tubular structures, was used for co-registration with immunofluorescent staining imaging using MATLAB R2019a software. 6052 single pixels from 19 different renal cell types were selected in SCiLS Lab 2016b according to their co-registration. Considering of the accuracy of the co-registration, we tried to avoid the pixels from the border area of the renal structures, only select

the pixels from the core of the renal structures. Peak intensities of the 544 *m/z* features were exported for each of the 6052 pixels and grouped into 19 cell types. This dataset was further used for uniform manifold approximation and projection (UMAP) analyses. For UMAP analysis, the datasets were transformed into a count matrix by multiplying the TIC-normalized intensities by 100 and taking the integer. This count data matrix was normalized and scaled using LogNormalize to generate a 2-dimensional UMAP map using Seurat (Stuart et al., 2019) in R (version 4.0). The differential abundance of lipids between clusters were analyzed using FindAllMarkers function in Seurat.

For the non-supervised lipid analysis, a total of 326 high molecular weight features (*m/z* > 400, predominately phospholipids, Table S1) that not co-localized with matrix peaks were selected (signal-to-noise-ratio > 3). The pixels from different MSI measurements of Human fetal kidneys and kidney organoids were directly exported from SCiLS Lab 2016b without immunofluorescent staining co-registration. For nephroblastoma samples, the pixels from blastoma cell areas were selected after co-registration and exported from SCiLS Lab 2016b. These datasets were transformed into a count matrix for UMAP analysis as described above. The distribution of the pixels from different clusters on tissues were co-registered to the IF staining, and cell types were identified based on both staining and their morphology on the tissue. The differential abundance of lipids between clusters were analyzed using FindAllMarkers function in Seurat. To compare pixels from different datasets, these matrices were imported into the Seurat package and a data integration step was performed after batch correction using the method provided by Seurat. To compare the pixels between kidney organoids and human fetal kidney, 16 WG human fetal kidney dataset was used as a reference for the integration of different kidney organoids dataset after batch correction. Only pixels from the annotated renal cells were used for data integration, which the pixels from gaps and undefined cells were filtered out. An integrated UMAP analysis was performed after data integration.

For dynamic metabolomics, the metabolite *m/z* features from the 16 WG human fetal kidney, so only lipid *m/z* features were left, which were used as query. Then the MALDI-MSI data from ^{13}C-labeling experiments of 17 WG, 18 WG and 19 WG human fetal kidneys were used as a reference to transfer metabolite production into the query using FindTransferAnchors and TransferData function from Seurat package in R. Both the query and reference were normalized and scaled using LogNormalize. Ultimately, all the imputed metabolite productions were combined into 16 WG dataset, which contained the ^{13}C-labeling information over time. The 13C-labeled metabolite abundance was corrected to its isotope tracer purity. Natural isotope abundance correction was performed for metabolites using R package IsoCorrectoR (Heinrich et al., 2018). After combining all the imputed data into one dataset and correcting the natural isotope abundance, the fraction enrichment of isotopologues was calculated based on the ratio of each ^{13}C-labeled metabolite (isotopologue) to the sum of this metabolite abundance in each pixel. The calculated fraction enrichment of isotopologues was used to generate pseudo-images together with pixel coordinate information exported from SCiLS Lab 2016b. The average fraction enrichment values (area under curve normalized to total time) of identified clusters were used for generating graphs and statistical analysis. Hotspot removal (high quantile 99%) were applied to all the pseudo-images generated from calculated values.

The data matrix of 16 WG fetal kidney or integrated data matrix of nephroblastoma with 16 WG fetal kidney from Seurat was further used to for the trajectory analysis using Monocle3 (Qiu et al., 2017) in R. The pseudotime scores were further used for Spearman's correlation analysis with lipids or metabolites. A spatial trajectory map was generated using MATLAB R2019a based on embedding information of UMAP and pseudotime values calculated by Monocle3 and pixel coordinate information exported from SCiLS Lab 2016b as descripted below.

For molecular histology, the datasets were used to generate 3-dimensional UMAP map using packages Seurat and plotly. The embedding information of 3-dimensional UMAP was translated to RGB color coding by varying red, green and blue intensities on the 3 independent axes. For spatial trajectory, the embedding information of 2D UMAP and pseudotime values was translated to RGB color coding by varying red, green and blue intensities on the 3 independent axes. Together with pixel coordinate information exported from SCiLS Lab 2016b, a MxNx3 data matrix was generated and used to generate UMAP images in MATLAB R2019a. A 3D scatterplot of the UMAP image was generated in MATLAB R2019a.

Single cell RNA-seq analysis

We used our preprocessed single cell transcriptomics data of 13WG, 16 WG and 18 WG kidneys from a previous report (Hochane et al., 2019). In short, single cells were isolated from human fetal kidneys, and scRNA-seq libraries were prepared using the Chromium Single Cell 3' Reagent Kit, Version 2 Chemistry (10× Genomics) according to the manufacturer's protocol. Libraries were sequenced on a NextSeq500 in Mid Output mode using a version 2, 150-cycle kit (Illumina). Single cell expression was quantified using unique molecular identifiers (UMIs) by 10× Genomics' ''Cell Ranger'' software. The dataset was further normalized and clustered to different cell types using R packages. For this study, All the detected genes were used to do pathway analysis in Reactome (https://reactome.org/), and all the genes involved in metabolism pathway (2066 genes) based on the Reactome were selected for further analysis. The differential expression of metabolic genes between cell types was analyzed using FindMarkers function in Seurat package in R. A cutoff (log2 fold change >0.75 and padj <0.05) was taken for further pathway analysis using Reactome. Heatmaps were produced using the R pheatmap package based on z-scores of genes expression from the clustered cell types. The 16 WG data matrix of metabolic genes from Seurat was further used to for the trajectory analysis using Monocle3 in R. The pathway activity score calculation was performed on all the genes of 16 WG dataset using testSctpa package in R. AUCell tool and Reactome database were used for the pathway activity score calculation. The pathway activity score and pseudotime score were further used for Spearman's correlation analysis.

The single cell transcriptomics data of hiPSC-derived kidney organoids was from our previous processed dataset (Koning et al., 2022). In short, single cells were isolated from kidney organoids differentiated from hiPSC-MAFB line at day 7 + 20. The single cell

suspensions were converted to barcoded scRNA-seq libraries with a targeted cell recovery of 9000 cells/condition using the Chromium Single Cell 3′ v3 Library, Gel Bead & Multiplex Kit and Chip Kit (10x Genomics). The scRNA-seq libraries were converted into DNA nanoballs (DNB) using a standard circularization protocol optimized for the DNBSEQ-T7 sequencer, and all subsequent steps were carried out following the standard operation procedure, as previously described (Huang et al., 2017; Korostin et al., 2020). The scRNA-seq libraries were sequenced aiming for at least 50,000 reads/cells, and using 28 + 100+8 bp paired-end sequencing to determine (1) the cell barcode and UMI, (2) the transcript and (3) the sample index, respectively. Demultiplexing according to the sample barcodes, and subsequent read alignment were performed using Cell Ranger (10x Genomics, v3.1.0). Raw unfiltered data matrices from the Cell Ranger output were then further processed with R and Seurat package. The dataset was used for renal cell classification using the developing kidney cell classifier (DevKidCC) (Wilson et al., 2022) in R. To compare the single cell transcriptomics data from kidney organoid and 16 WG human fetal kidney, a data integration step was performed after batch correction using the method provided by Seurat.

Nuclear magnetic resonance (NMR) metabolomics

For NMR measurement, 0.2 mL of culture medium was collected and mixed with 0.4 mL of cold (−80°C) 100% LC-grade methanol to extract extracellular metabolites. All samples were subsequently placed at −80°C for at least 30 min and centrifuged for 20 min at 18,000 × g, at 4°C. The supernatants from culture medium extracts were collected and dried with nitrogen gas. NMR samples of extracts were prepared by dissolving the dried material with 0.22 mL of 0.15 M phosphate buffer (pH 7.4) in deuterated water containing 0.05 mM trimethylsilyl propionic-*d*4-sodium salt (TSP-*d*4) as internal standard for NMR referencing and quantification. An 1D ^{1}H-NMR spectrum was collected for each sample on a 14.1 T (600 MHz for ^{1}H) Bruker Avance II NMR, using the 1D-NOESY experiment with presaturation as implemented in the spectrometer library (Topspin v3.0, pulse sequence: *noesygppr1d*; Bruker Biospin, Ltd). All spectra were processed to correct the phase and baseline and imported in Chenomx NMR suite 8.4 (Chenomx NMR suite, v8.0, Edmonton, Canada) for quantification of metabolites.

QUANTIFICATION AND STATISTICAL ANALYSIS

Statistical analysis were performed using GraphPad Prism 8 and data are presented as mean ± SD, unless indicated otherwise. Data normality and equal variances were tested using Shapiro-Wilk test. Differences between two groups were assessed by paired 2-tailed Student's *t* test or one sample t-test, and between multiple groups were assessed by one-way ANOVA followed by Tukey test. If the data were not normally distributed or not of equal variance, the Mann-Whitney *U* test was performed. p-value < 0.05 were considered statistically significant.